Dynamically Formed Active Sites on Liquid Boron Oxide for Selective Oxidative Dehydrogenation of Propane

Jinshu Tian[1,2,3,#], Gregory Collinge[1,#], Simuck F. Yuk[1,4], Jingdong Lin[3], Wei Shao[2], Vassiliki-Alexandra Glezakou[1], Mal-Soon Lee[1]*, Yong Wang[1,5]*, and Roger Rousseau[1]*

[1] Institute for Integrated Catalysis, Pacific Northwest National Laboratory, Richland, WA 99354, USA
[2] College of Chemical Engineering, Zhejiang University of Technology, Hangzhou 310014, China
[3] College of Chemistry and Chemical Engineering, Xiamen University, Xiamen 361005, China
[4] Department of Chemistry and Life Science, United States Military Academy, West Point, NY 10996, USA
[5] Voiland School of Chemical Engineering and Bioengineering, Washington State University, Pullman, WA 99164, USA

***Corresponding Authors:** malsoon.lee@pnnl.gov (M.-S. Lee); Yong Wang, wang42@wsu.edu (Y. Wang), roger.rousseau@pnnl.gov (R. Rousseau)

[#] These authors contributed equally.

Abstract: Boron-based catalysts have been shown to be both active and selective for driving the oxidative dehydrogenation of propane (ODHP) without the use of metal promoters. However, this reaction occurs at temperatures where the oxide catalyst melts which challenges our ability to identify the liquid structures of the boron oxide phase under reaction conditions, hindering the understanding of its active sites and reaction mechanism. By combining *ab initio* molecular dynamics simulations, *in situ* Raman characterization, and microkinetic modeling, we propose that the di-coordinated boron sites (>B*) in liquid boron oxide are the active species for O_2 activation under reaction conditions. This peroxy-like species (>B-O-O-B<) can be viewed as a moderate oxidant for ODHP, reactive to propane but inert to propene. The dynamical >B-O* dangling bonds, originating from the >B-O-O-B< site as well as the liquid B_2O_3 structure itself, play a critical role in the abstraction of H atoms from propane (adsorbed C_3H_7* radical formation). In fact, microkinetic modeling reveals that the formation of adsorbed C_3H_7* radicals is the main rate controlling step (~75% rate control) with the dehydration of boron hydroxyls to recover the di-coordinated >B* active sites controlling the remainder of the rate (~25% rate control). Moreover, the activation barriers are found to strongly depend upon the surface B-OH concentration. These findings provide significant insights into the active sites and reaction mechanisms of ODHP on boron-based catalysts and emphasize the importance of understanding and accurately modeling the liquid nature of the catalyst to account for its catalytic activity.

Keywords: liquid B_2O_3; oxidative dehydrogenation of propane, di-coordinated boron site; dehydration of hydroxyls.

Introduction

Boron-containing materials (h-BN, BNOH, B_4C, TiB_2, NiB, WB, Co_2B/Co_3B, HfB_2 and BS-1)[1-6] and supported boron oxides (B_2O_3/SiO_2 and B_2O_3/Al_2O_3)[7-10] are potential catalysts for oxidative dehydrogenation of propane (ODHP). Their interest stems from the fact that these catalysts show reasonable activity and excellent selectivity yet do not require a precious or transition metal as is ubiquitously employed for hydrocarbon transformations.[11-13]. Hence these materials offer the tantalizing prospect of being able to employ catalysts based on earth abundant and cost-effective materials.

The origin and identity of the ODHP active site and the dominant ODHP reaction mechanism over these boron-based catalysts are still under intense debate. *Grant et al.* initially suggested that a >B-O-O-N< structure was the active site for ODHP over h-BN catalysts[1]. This statement was later contradicted by the observation of an oxidized boron phase (BO_x), which was generated on the surface of boron-containing materials after the ODHP reaction.[2] Further structure analysis led to the proposition that the active sites are instead surface-formed amorphous species like $B_2(OH)_{2x}O_{(3-x)}$ (x = 0-3).[14-15] Taken together, this suggests that it is a nitrogen-free boron oxide that is the active phase. On the other hand, *Shi et al.* studied the hydroxylated h-BN as ODHP catalyst and suggested that it is the hydroxylated B-OH groups at the edges of h-BN that are the active sites for ODHP,[3, 16] suggesting once again that boron nitride is involved indirectly. However, further research by *Lu et al.* on non-nitride B_2O_3/SiO_2 catalysts seems to contradict involvement from the boron nitride phase as such catalysts are shown to be ODHP active despite the lack of nitrogen.[8] These authors posited that it is the hydroxylated boroxol ring/tri-coordinated planar oxidized boron species that are the active sites and proposed that the B-OH sites react with molecular oxygen (which they postulate is the rate-limiting step) to produce >B-O-O-B< sites[16-17] or >BO*-OH intermediates[8] that can abstract the hydrogen atoms from propane. Additionally, *Zhou et al.* discovered an isolated boron -B[OH--O(H)--Si]$_2$ structure in a zeolite framework that exhibits high activity and selectivity for ODHP,[4] strongly suggesting that the active site is indeed a BO_x-type species. Despite this, the identity and structure of this species/site, and its molecular role in observed ODHP are unknown, let alone agreed upon.

The remarkable product distribution on these boron-based catalysts was rationalized by Vengas et al. as a combination of surface-mediated formation of radicals (HOO* radicals) over metastable sites (BO_x site) and their sequential propagation in the gas phase (HOO* radicals and propane).[18] In that work, the water assisted surface regeneration reaction ($2BOH \xrightarrow{H_2O} BO^* + B^* + H_2O$) was stated to be the rate-limiting step. Similarly, the latest research has confirmed that a gas-phase free radical reaction over h-BN catalysts occurs during ODHP[18-20]. Specifically, *Zhang et al.* demonstrated that propene is mainly generated on the catalyst surface (BO_3 site) from the C-H activation of propane (proposed as the rate-limiting step) following a Langmuir-Hinshelwood mechanism, while C_2 and C_1 products are formed via both surface-mediated and

gas-phase pathways.[20] This was described in our previous report, as well.[21] Peter et al. further stated that a high selectivity toward propene and ethene is fully consistent with a gas-phase conversion mechanism on the boron nitride catalyst, where the catalyst is only responsible for initiating the gas-phase chemistry.[19] Nonetheless, a surface reaction mechanism is far from ruled out. Thus, despite considerable research, the nature and origin of the active site(s) under reaction conditions and corresponding reaction mechanisms remain unclear and need to be further clarified.

One major challenge which hinders progress for both experimental and theoretical studies is that ODHP catalysis is typically performed on a molten oxide which does not have a fixed, well-defined structure. More specifically, the B_2O_3 active phase, with a melting point of ~725 K[22], is in a liquid state at OHDP reaction temperatures (>800K). It is thus difficult for *ex-situ* characterization to identify the actual active sites of the boron-based catalyst during the reaction, resulting in the disparate models describing ODHP active sites and reaction mechanisms.[4, 8, 14, 16, 18, 20, 23-27] Even with *in situ* experiments, it is difficult to detect short-lived intermediates, which may also be in relatively low concentration but are nonetheless critical for understanding catalysis. Studies have shown that the dynamic process under real reaction conditions would benefit from computational investigations of metastable surface sites[18, 23, 28-32] beyond thermodynamically stable species such as tri-coordinated boron species (>B-) and boron hydroxyls (B-OH).[18, 23] This requires that one takes into account the mobility of sites and species, collective dynamics, and larger anharmonicities which are often neglected in computational models based on static structures and which can have significant impact on computed reaction free energies[33]. *Ab initio* molecular dynamics (AIMD) along with enhanced sampling methods[34], such as Blue Moon ensemble techniques or metadynamics simulations, are powerful tools to provide this type of quantitative information on the atomic-scale structural properties of the catalysts and the intermediate species under real reaction conditions.[35-37] However, even this approach is not sufficient for probing this phenomenon theoretically. For liquid catalysts, one must also account for long time scale phenomena such as flexibility of catalyst structures, sites, and active species which are critical for the kinetics, and hence a microkinetic ansatz that captures features unique to the liquid state is mandatory.[38-39]

Herein, by combining AIMD simulations along with an enhanced sampling method for modeling reaction free energetics, microkinetic modeling, and *in situ* experiments, we have elucidated the active sites and reaction mechanism on boron-based catalysts under OHDP reaction conditions. The AIMD simulation and *in situ* Raman spectra reveal the presence of di-coordinated boron radical species (>B* site) in the liquid B_2O_3 phase, which we show activate dioxygen molecules to form peroxide-like >B-O-O-B< sites. The C_3H_8 molecules are gently oxidized from the gas phase at a >B-O-O-B< site, forming a C_3H_7* radical loosely bound to newly formed B-OH. The dynamically formed >B-O* dangling bond plays a key role in the subsequent dehydrogenation reaction while also being very active for C_3H_8 activation, as well.

Importantly, Blue-Moon ensemble simulations show that the free energetics of recovering active sites via the dehydration of surface B-OH is strongly dependent upon B-OH concentration, resulting in coverage dependent thermodynamics and kinetics. These results were then used to parameterize a novel microkinetic model of ODHP over liquid phase B_2O_3, whose solution reveals C_3H_7* radical formation to be the primary rate controlling step. This is found to be due to the poor adsorption strength of propane at elevated temperatures, which makes the formation of the much more stable C_3H_7* radical the critical step in ensuring forward reaction flux. Recovery of the >B* active site via dehydration of B-OH is found to control the remainder of the ODHP rate as we find this to be the only activated process in the reaction mechanism at 850 K. The model compares favorably with previously reported kinetics and supports the assertion that dynamical processes are critical for understanding the activity of liquid phase catalysts.

Results and Discussion

Formation and micro-structure of the liquid B_2O_3 using AIMD simulations

At 850 K during ODHP, the B_2O_3 should be in a liquid phase (melting point ~725 K), suggesting that its structure and physical properties will deviate significantly from the solid phase. To obtain a liquidized B_2O_3 phase, we first carried out AIMD simulations above the melting point starting from the low-pressure crystalline polymorph B_2O_3-I phase,[40-42] whose computed and experimental lattice parameters can be found in Table S1. Using a supercell of 480 atoms, an exceptionally high temperature was applied (2000 K for ~12 ps) to melt the oxide into a completely disordered state, where correlation to its initial configuration vanishes. Once disorder was established, we gradually decreased the temperature of the system to the target temperature of 850 K, where the system was then equilibrated by running for another ~20 ps (Figure S1). The simulation revealed that the atomic structure of boron oxide underwent a rearrangement from an ordered to a disordered state (Figure S2). We also performed mean square displacement analysis (MSDs) (Figure S3) to confirm this. The corresponding diffusion coefficients for boron atoms ($D_{(B)}$) and oxygen atoms ($D_{(O)}$) are calculated to be ~7.5×10^{-7} and 8.0×10^{-7} cm^2/s, which is consistent with those found in previous molecular dynamics simulations of molten systems.[43-44]

In addition, to elucidate the cleavage and regeneration of the >B-O-B< bonds in liquid B_2O_3 phase, the details of the AIMD trajectory were analyzed (Figure S4-S6). AIMD simulations produce a system exhibiting (i) the formation of boroxol rings (Figure S4) which typically only exist in the amorphous and liquid B_2O_3 phase,[41-42] and (ii) the cleavage of the highly stable >B-O-B< bonds, forming two-coordinate >B* species and >B-O* dangling bonds (Figure S5 and S6), which have been reported to be active in the ODHP reaction[23].

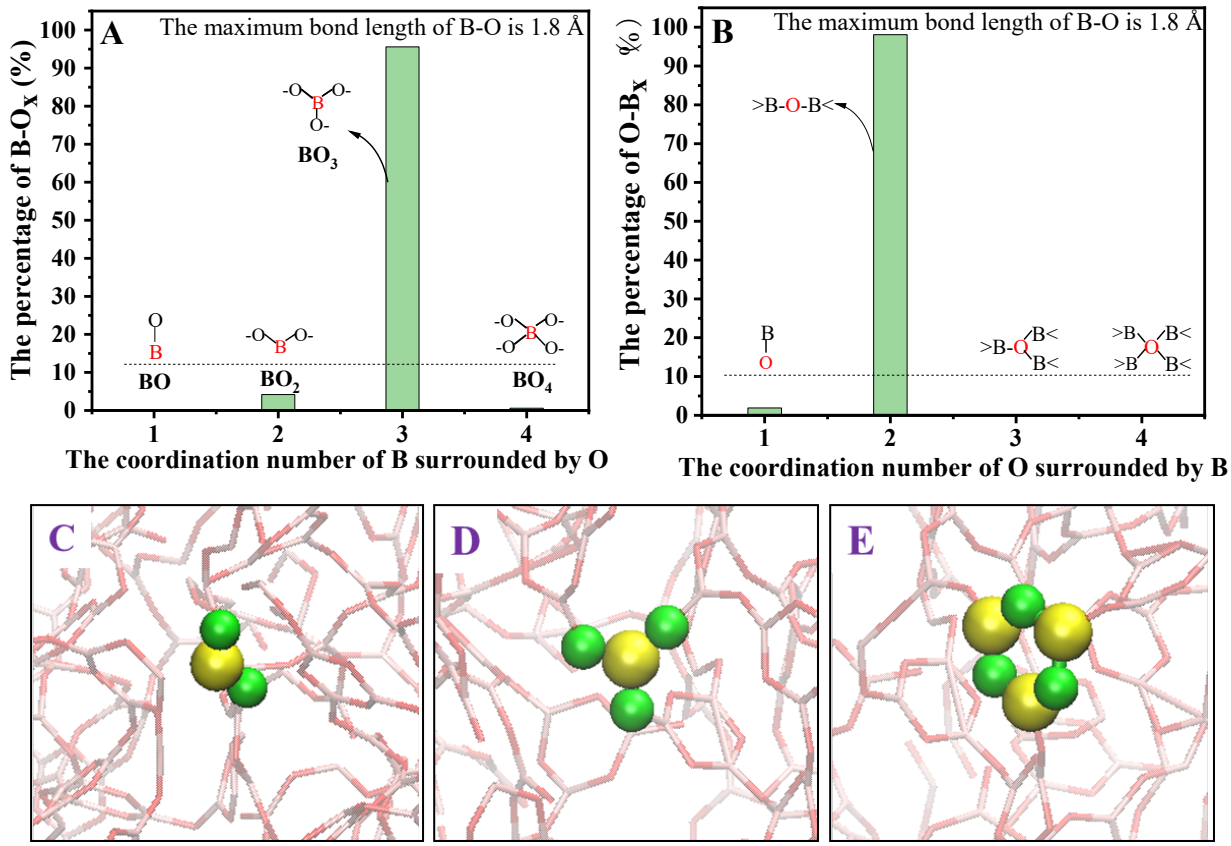

Figure 1. Coordination number analysis of boron and oxygen atoms in liquid B_2O_3 at 850 K. (A): the coordination number of boron atoms surrounded by oxygen atoms; (B): the coordination number of oxygen atoms surrounded by boron atoms; Corresponding structures for (C): di-coordinate >B* sites; (D): tri-coordinate >B- species; and (E): B_3O_6 rings. Yellow spheres represent boron atoms; green spheres represent oxygen atoms.

To probe the structures within the simulated liquid B_2O_3 phase, we analyzed the distribution of boron and oxygen coordination environments (Figure 1 and Figure S7). Coordination numbers (CN) were computed using a B-O bond length of 1.8 Å, derived from the first minimum of the B-O bond radial distribution function. The distributions of boron and oxygen CNs are displayed in Figure 1A and Figure 1B, respectively. It is found that ~95% of boron atoms are tri-coordinate (>B-) with the remaining ~5% being primarily di-coordinate, representing >B* species. A very small fraction of boron atoms are tetra-coordinate (>B<), and none are mono-coordinate, consistent with the literature.[42, 45] The corresponding breakdown for oxygen atoms shows that they are primarily (>95%) di-coordinate >B-O-B< species/bonds, while very small fraction of them are tri- and tetra-coordinate. About ~1.5% of oxygen atoms are mono-coordinate, and we can identify each of these atoms as one >B-O* dangling bond. Interestingly, however, since a di-coordinate >B* species (~5% of boron atoms) is created along with each >B-O* dangling bond (Figure S6), one would expect closer to ~5% of the total boron atoms to be in >B-O* dangling bonds, too. We would thus expect ~3.33% of the total number of oxygen atoms to be in >B-O* dangling bonds, yet we have

computed a value that is just under half that (~1.5%). The lowered content of the >B-O* dangling bond is due to the high activity of its oxygen radical, which for the grand majority of oxygen atoms simply results in dynamic re-generation of the >B-O-B< bond via recombination with a >B* site (Figure S8). However, for a small minority, the oxygen radical may also attach to a tri-coordinated >B- species to form the observed tetra-coordinated >B< species or to another >B-O* dangling bond to form a peroxy-type species that will be expounded upon later. This results in the consumption of just over half of the >B-O* dangling bonds produced by the cleavage of the >B-O-B< bonds in our simulation. Nevertheless, the dynamic formation of >B-O* dangling bonds promotes the reaction as will be discussed below. Interestingly, the >B* sites on the surface of liquid boron oxide always appears in pairs (Figure S9), which is closely related to the energy minimization of the entire system. A mole balance coupled to the above analysis allows us to extract an estimate of each BO_x species' population at 850 K, enabling the quick evaluation of their equilibrium constants (to within approximately an order of magnitude). These equilibrium constants are used to define elementary reactions reflective of the dynamic formation of active sites during reaction.

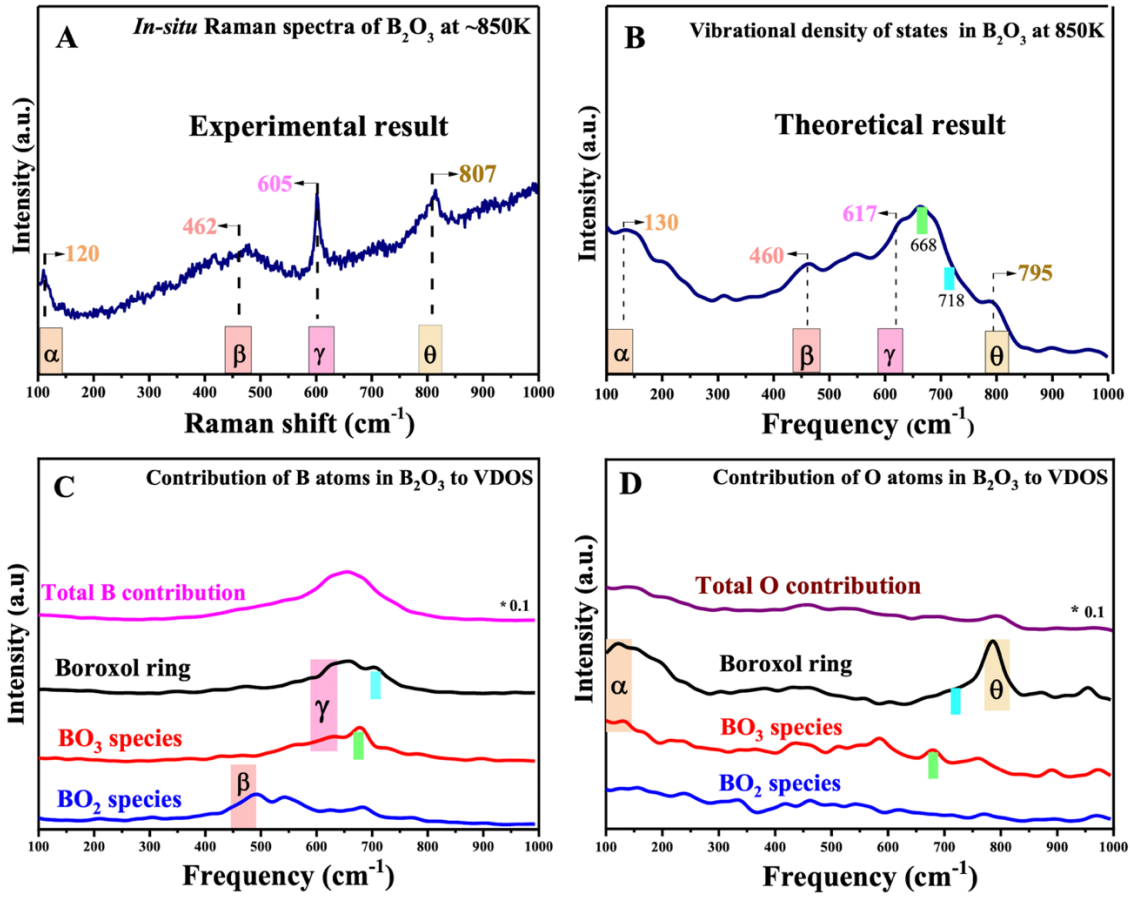

Figure 2. (A-B) I*n-situ* Raman spectra and the vibration density of states (VDOS) of liquid B_2O_3 at ~850 K, respectively. (C-D) The contribution of boron and oxygen atoms to the VDOS, respectively. Shaded regions labeled α, β, γ, and θ designate areas in the local VDOS spectra that match to peaks in the *in situ* Raman spectrum.

The structure of the liquid B_2O_3 was also probed using the *in situ* Raman at ~850 K under N_2 conditions and the results are shown in Figure 2(A). There are four main peaks at 120, 462, 605, and 807 cm^{-1} which are respectively labeled as α, β, γ and θ. Figures 2B-2D show the computational vibrational density of states (VDOS) of liquid B_2O_3, and corresponding contributions of boron and oxygen at 850 K, respectively. Most peaks in the VDOS are found to align well with those in the *in situ* Raman spectrum, allowing us to designate the α, β, γ and θ peaks on a one-to-one basis. Other peaks are evident in the VDOS, but these are assumed to correspond to Raman inactive species. The α peak at ~130 cm^{-1} (10 cm^{-1} deviation from Raman) is found to represent the oxygen atoms in both boroxol rings and >B- sites. The β peak at ~460 cm^{-1} (Figure 2B, 2 cm^{-1} deviation) represents the contribution of boron from the di-coordinated >B* sites while the γ peak at ~617 cm^{-1} (12 cm^{-1} deviation) represents the contribution of boron from both boroxol rings and tri-coordinate >B- species. The θ peak at ~795 cm^{-1} (12 cm^{-1} deviation) is attributed to the oxygen in boroxol rings. Combining the VDOS and *in situ* Raman spectra, we can conclude that the peaks at 807 and 462 cm^{-1} (Figure 2A) can be attributed to the contribution of boroxol rings and di-coordinate >B* sites, respectively. The peaks at 605 and 120 cm^{-1} mainly come from the contribution of both tri-coordinate >B- species and boroxol ring sites, whereas the peaks at 668 and 718 cm^{-1} (Figure 2B), can be attributed to the vibrations of $(BO_3)_3$ "triangles" and boroxol rings, respectively,[46] but are not observed in *in situ* Raman spectra due to being Raman inactive. These VDOS data further confirms that our molecular model of liquid B_2O_3 accurately reflects its liquid state.

Reaction mechanism for ODHP on liquid B_2O_3.

Based on the above analysis of the structure of liquid boron oxide, there are three possible O_2 adsorption sites under reaction conditions: a di-coordinate >B* site, a tri-coordinate >B- site, and a boroxol ring site. To probe their susceptibility to the ODHP reactants, we calculated the Bader charges[47-51] of these three sites on liquid boron oxide. The calculated Bader charges of boron in the >B* site, boroxol ring, and >B- species are ~2.5, ~3.0, and ~3.0 $|e^-|$, respectively, indicating some diversity in boron chemical environments (Figure S9A-S9B). To determine if any of these sites' electrons are unpaired and therefore likely to exhibit strong chemical binding and orbital rehybridization, we computed the projected density of states (PDOS) for each site and then separate the spin up from the spin down states to inspect their parity. Considering the PDOS for all boron atoms in B_2O_3 (Figure S10), there is almost exact parity except at an energy level of 0.3 eV, which we can conclude are from the contribution of >B* sites as evidenced by the unpaired peaks around this energy level in its local density of states (Figure S9C). This result implies that >B* sites may be the most active site among the three possible.

Starting from these three potential O_2 adsorption sites, we conducted a detailed exploration of the reaction mechanism in ODHP. It is widely accepted that oxygen should first adsorb onto the boron oxide surface, forming active sites for further activation of propane. We calculated the adsorption energy of

oxygen at different O_2 adsorption sites (Figure S11 and Table S2). The adsorption of oxygen on the >B* site is very exothermic (-2.43 eV) while adsorption on the other two sites is unfavorably endothermic (0.51 and 0.76 eV). This result is consistent with Bader charge and PDOS analyses. Once the O_2 is adsorbed and activated on the >B* site, the aforementioned bridging peroxy-type species is formed as shown in Figure 3 and denoted as >B-O-O-B<. The bridging oxygen atom Bader charges in >B-O-O-B< are ~1.0 $|e^-|$ each, identifying this as an inorganic peroxide species that should be capable of performing oxidation reactions. Starting from this peroxy active site (>B-O-O-B<), we then calculated key intermediates for the ODHP reaction.

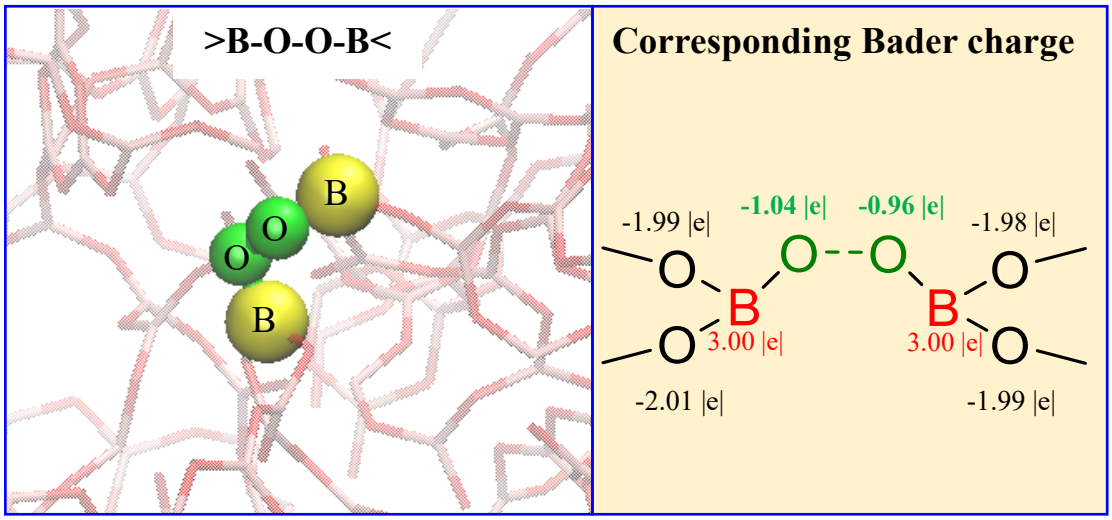

Figure 3. The structure analysis of >B-O-O-B< forming by the interaction between O_2 and >B* sites.

As shown in Figure 4A, the beta C-H bond of C_3H_8 first undergoes a redox reaction at the >B-O-O-B< site forming a C_3H_7* radical bound to the boron of a newly created B-OH species and the formation and release of a >B-O* dangling bond through a simultaneous cleavage of the >B-O-O-B< site. AIMD shows that the propane activation at >B-O-O-B< sites is spontaneous, requiring a mere ~0.1 ps at 850 K to react. In this simulation, after another ~2.4 ps of AIMD, the thus formed B-OH bound C_3H_7* radical further interacted with a nearby coordinatively-unsaturated oxygen site (Bader charge, ~1.75 $|e^-|$), specifically the oxygen atom of a tetra-coordinated boron (>B<), to produce an adsorbed C_3H_6 molecule and a second B-OH (Figure 4B). Such lifetimes correspond to extraordinarily large turnover rates. The adsorbed propene is stable against further oxidation at 850 K, with no further reaction being observed after ~9.0 ps (Figure S12) of AIMD, demonstrating that the >B-O-O-B< site is indeed a mild oxidant.

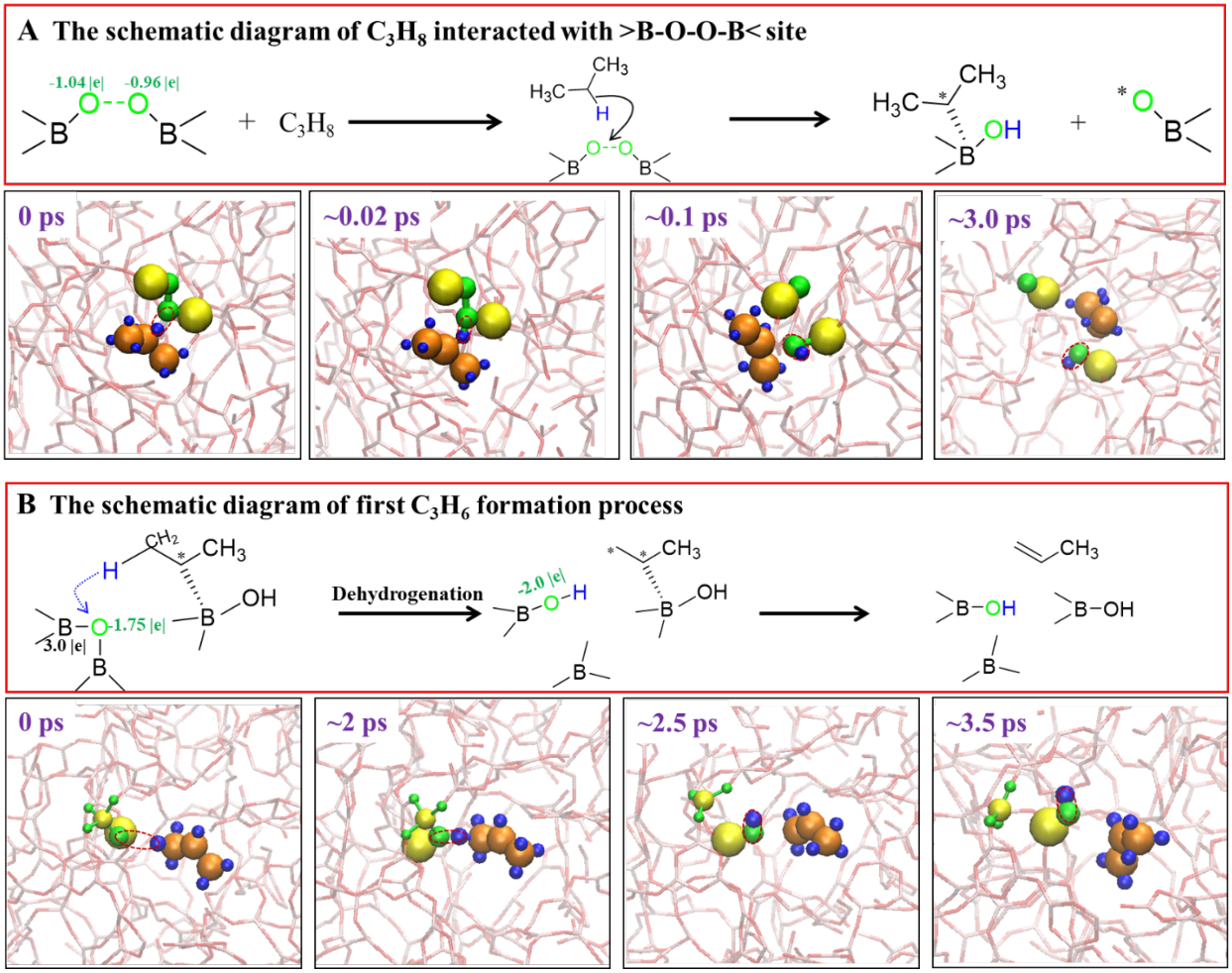

Figure 4. The schematic diagram and corresponding selected snapshots of the AIMD trajectory for (A) the C_3H_8 activation by >B-O-O-B< site; (B) the first C_3H_6 formation process. Yellow balls represent boron atoms; Green balls represent oxygen atoms; Orange balls represent carbon atoms; Blue balls represent hydrogen atoms.

To complete the catalytic cycle, a second propane must be oxidatively converted to propene as well. This is shown in Figure 5, where the beta C-H of the propane is abstracted by the highly active >B-O* dangling bond active site, forming B-OH and C_3H_7* species in a remarkably short time (~0.02 ps). For the dehydrogenation process of C_3H_7* species, if the catalyst is in a solid state with relatively fixed active sites, the subsequent and final dehydrogenation reaction is exceedingly slow. However, in the liquid state the surface structure is more flexible and dynamic[23] and this impediment to reactivity is removed. A high-temperature AIMD simulation at 2000 K (to shorten the run time) on hydroxylated boron oxide confirms that >B-O* dangling bonds and di-coordinated >B* species are dynamically formed and have a certain fluidity on the surface of the liquid B_2O_3 phase, regardless of hydroxylation. Based on this, we further investigated the activation process of C_3H_7* species by >B-O* dangling bonds (Figure S13) at 850 K. The presence of the >B-O* dangling bond quickly prompts immediate reaction to form B-OH and the second propene molecule. In short, we found that there are no or very low reaction free energy barriers for all

dehydrogenation steps of propane. Our results indicate that propane can be activated quickly and spontaneously in the liquid state by either >B-O-O-B< active sites, tetra-coordinated >B< species, or >B-O* dangling bonds with practically equal alacrity. This suggests that reactivity strongly depends on the adsorption probability of propane at these sites as subsequent steps are rapid and facile.

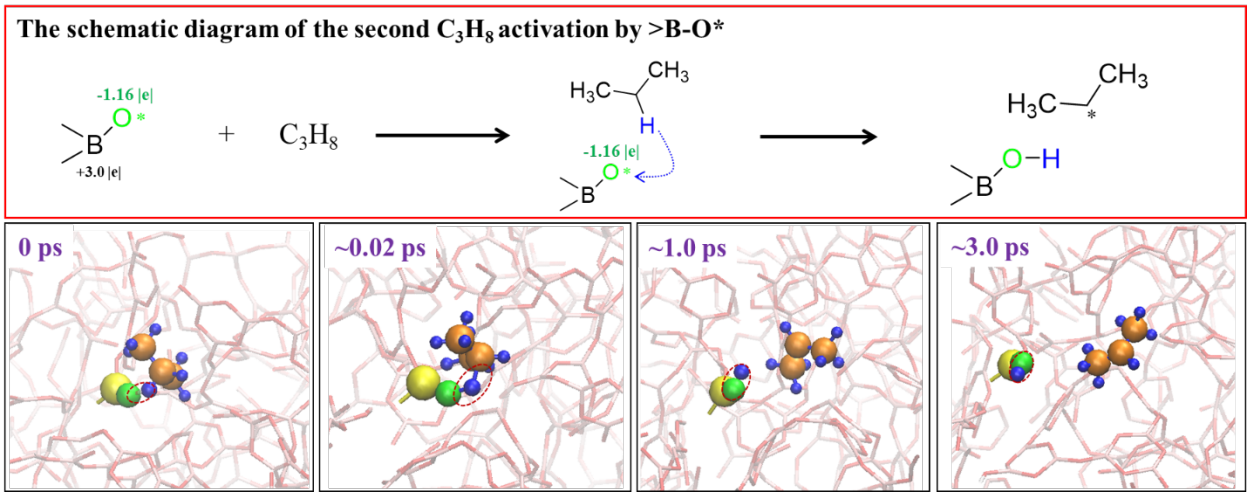

Figure 5. The schematic diagram and corresponding selected snapshots of the AIMD trajectory for the C_3H_8 activation by >B-O* from the cleavage of >B-O-O-B< site. Green balls represent oxygen atoms; Orange balls represent carbon atoms; Blue balls represent hydrogen atoms.

Up to this point, we have elucidated the fate of two propane molecules and one oxygen molecule (a stoichiometric ratio for the overall ODHP reaction) with the corresponding elementary reactions leading to the formation of two propene molecules and four B-OH species. As mentioned above, AIMD simulations demonstrate that this process is spontaneous without appreciable free energy barriers at 850 K. However, while propene easily desorbs, the 4 B-OH (corresponding density: 1.22 B-OH/nm^2) are chemically stable on the liquid boron oxide surface (Figure S14), which is consistent with previous observations[18, 52] as well as our own experimental results (Figure S15). This suggests that active site regeneration via the dehydration of B-OH on the boron oxide surface is activated, consistent with previous assertions that this step may be rate limiting[18]. We rationalize that more propane turnovers would thus occur before these first B-OH species have a chance to dehydrate, implying that the density of B-OH would increase and change the chemical environment. We therefore ran further AIMD simulations with increasing density of surface B-OH to examine whether such a coverage change might affect the favorability of H_2O formation and desorption. At coverages of 2.45 and 3.67 B-OHs/nm^2, we indeed observe the spontaneous formation of adsorbed H_2O and a >B-O* dangling bond from two B-OH species within ~2.0 and ~1.0 ps of AIMD, respectively (Figures S16 and S17). However, at this B-OH density, the H_2O does not desorb before quickly dissociating again to form the B-OH species again. This suggests that proton dynamics and hydroxyl migration play a pivotal role in the desorption of H_2O. When the density of surface B-OH is further increased to 4.28 B-OH/nm^2,

we observe H_2O formation at ~0.15 ps to recover a >B-O* dangling bond and then finally desorption from the surface at ~1.0 ps (Figure S18) to recover the di-coordinated >B* active site to close the catalytic cycle. Taken together, these observations lend credence to the hypothesis that the regeneration of the active sites via the dehydration of B-OH is a controlling factor in the rate for ODHP on liquid boron oxide and strongly depend on the surface B-OH density.

Since the formation and desorption of H_2O is activated, we turn to Blue-Moon ensemble AIMD simulations (Figure S19-S24) to determine their activation free energy barriers at 850 K. Figure 6 shows the Gibbs free energy (ΔG) associated with H_2O formation via B-OH dehydration on the liquid boron oxide at 850 K. (As shown by *Collinge et al.*, the Gibbs free energy of volume-independent reactions like these is equivalent to the Helmholtz free energy (see its SI)[53], which simplifies computation). For the formation of H_2O, we found that, as the hydroxyl density increases (1.22 to 3.67 B-OH/nm^2), the activation free energy decreases from 1.65 to 0.31 eV, and the corresponding reaction equilibrium constant (k_F/k_R) increases from 1.6×10^{-10} to 1.5×10^{-2}. For the desorption of H_2O (Figure S23), the trends are similar to the formation of H_2O: the activation free energy decreases from 3.4 eV to a mere 0.28 eV and the equilibrium constant increases from 1.4×10^{-18} to 2.2×10^{-1}. This result is in line with previous experiments[52] where a positive linear relationship between the overall reaction rate and the density of OH species was reported (albeit in the transient regime). In addition, the Gibbs free energies (ΔG) of H_2O formation and desorption were decomposed into enthalpic, ΔH, and entropic, ΔS, contributions (Figure S24). As hydroxyl density increases, a significant increase in ΔS effectively cancels out and overtakes a concomitant increase in ΔH, resulting in an overall decrease in ΔG for the H_2O formation step while both entropy and enthalpy become more favorable in the H_2O desorption step, reemphasizing the important role of entropy over liquid B_2O_3 catalysts.[33]

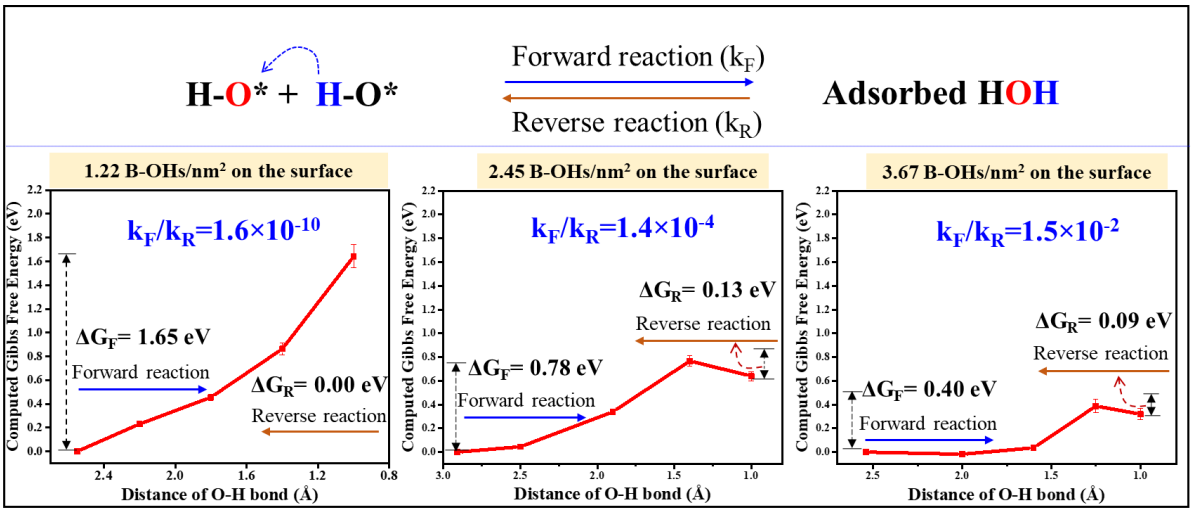

Figure 6. Computed Gibbs free energy (ΔG) profile and equilibrium constant (k_F/k_R) of the H_2O formation via B-OHs dehydration with different hydroxyl density on the surface (~1.22, ~2.45 and ~3.67 B-OH/nm^2).

Microkinetic model of oxidative dehydrogenation of propane (ODHP) on liquid B_2O_3

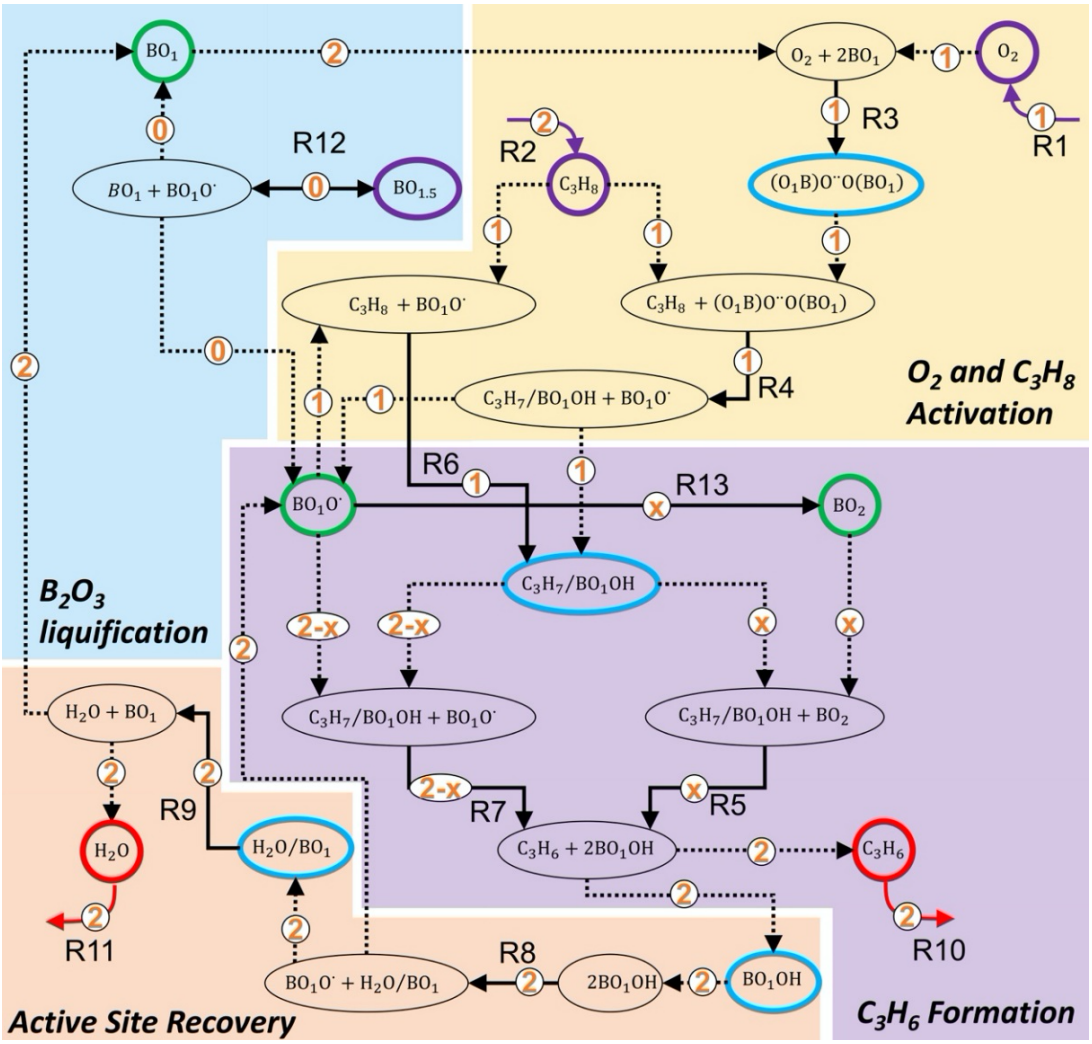

Figure 7. Reaction network of ODHP over liquid B_2O_3. Full black connector arrows represent elementary reaction steps while dashed black connector arrows represent the instantaneous availability of constituent intermediates within the underlying mean field approximation. Orange numbers in white circles represent the relative forward molecular fluxes of each reaction step at steady state with "x" being an unknown that arises due to the splitting of flux across parallel reactions R5 and R7. Purple, red, blue, and green bold circles distinguish between reactants, products, intermediates, and B_2O_3-derived species. Unconnected arrows represent reactions connecting the system to the gas phase.

Based on the preceding results, we can now assemble a plausible ODHP catalytic mechanism that accounts for the liquid nature of the B_2O_3 catalyst and its dynamic formation and recovery of active sites/structures (as observed in our AIMD simulations). Here we directly incorporate the various BO_x species that make up the liquid B_2O_3 catalyst as intermediate species, treating them no different than one would treat a molecular intermediate derived from the reactants. The overall reaction network is shown in Figure 7. The elementary reactions in this network are shown in Table 1 along with their forward and reverse activation free energy barriers, which were derived from the preceding AIMD simulations and used to

parameterize rate expressions (Table S3) needed to construct a mean-field ODHP microkinetic model (MKM). Note that we write all species in their stoichiometric form hereafter, where twice-bonded O atoms contribute 0.5 O to each BO_x species. This ensures that our elementary reactions (labeled "RX" for each reaction X) are stoichiometrically balanced. In the following text, species in their stoichiometric form are bolded to enhance their distinction. The overall reaction begins with the dynamic formation of $\mathbf{BO_1O^\bullet}$ (>B-O* dangling bond) and $\mathbf{BO_1}$ (>B* di-coordinated boron) active sites from two $\mathbf{BO_{1.5}}$ (tri-coordinated boron, ">B-") (see R12 in Table 1). This can then be followed by impingement of the catalyst surface by the reactants, $\mathbf{O_2}$ (R1) and $\mathbf{C_3H_8}$ (R2). $\mathbf{O_2}$ is activated by two $\mathbf{BO_1}$ active sites to form the peroxy $\mathbf{(BO_1)_2\ O_2}$ (>B-O-O-B<) species (R3). This peroxy species can then activate $\mathbf{C_3H_8}$ by dehydrogenation to form $\mathbf{C_3H_7/BO_1OH}$ with the $C_3H_7^*$ intermediate bound to a boron hydroxyl species, (R4), which also results in the formation and release of a $\mathbf{BO_1O^\bullet}$ active site. $\mathbf{C_3H_7/BO_1OH}$ is subsequently dehydrogenated by a $\mathbf{BO_1O^\bullet}$ (R7) or $\mathbf{BO_2}$ (tetra-coordinated ">B<", R5), but $\mathbf{BO_2}$ is only formed by attachment of $\mathbf{BO_1O^\bullet}$ to a nearby $\mathbf{BO_{1.5}}$ (R13). This makes R5 and R7 parallel reactions even though we encountered them sequentially in our AIMD simulations. The first dehydrogenation of propane to form $\mathbf{C_3H_7/BO_1OH}$ can also occur via the $\mathbf{BO_1O^\bullet}$ active site (R6). The final dehydrogenation of $\mathbf{C_3H_7/BO_1OH}$ (whether by R5 or R7) produces adsorbed propene, $\mathbf{C_3H_6}$, and two $\mathbf{BO_1OH}$ (B-OH). With sufficient coverage, two $\mathbf{BO_1OH}$ can couple to form >B* bound water, $\mathbf{H_2O/BO_1}$, and recover a $\mathbf{BO_1O^\bullet}$ active site (R8). The favorability of the subsequent separating/releasing of $\mathbf{H_2O}$ to recover a $\mathbf{BO_1}$ active site (R9) is also facilitated with higher $\mathbf{BO_1OH}$ coverage. The catalytic cycle is then closed upon desorption of two $\mathbf{C_3H_6}$ and two $\mathbf{H_2O}$ molecules (R10 and R11, respectively).

Table 1. Elementary reactions along with their forward and reverse activation and reaction free energies used to parameterize the liquid phase B_2O_3 ODHP MKM developed here. We differentiate between the gas- and adsorbed phase of reactant and product molecules with labels "(g)" and "(a)", respectively.

Rxn #	Elementary Reaction	Description	$\Delta G^{\ddagger}_{i,fwd}$ (823 K) [eV]	$\Delta G^{\ddagger}_{i,rev}$ (823 K) [eV]	ΔG_i (823 K) [eV]
Propane Oxidative Dehydrogenation Cycle					
R1	$O_2(g) \rightleftharpoons O_2(a)$	O_2 Impingement	unactivated	unactivated	-0.149
R2	$C_3H_8(g) \rightleftharpoons C_3H_8(a)$	C_3H_8 Impingement	unactivated	unactivated	0.505
R3	$O_2(a) + 2BO_1 \rightleftharpoons (BO_1)_2O_2$	O_2 activation by BO_1 Active Site	k_BT	$k_BT + \Delta G_3$	-1.698
R4	$C_3H_8(a) + (BO_1)_2O_2 \rightleftharpoons C_3H_7\text{-}BO_1OH + BO_1O^\bullet$	C_3H_8 Activation: Dehydrogenation by Peroxo Active Site	k_BT	$k_BT + \Delta G_4$	-0.583
R5	$C_3H_7\text{-}BO_1OH + BO_2 \rightleftharpoons 2BO_1OH + C_3H_6(a)$	Final Dehydrogenation (with BO_2)	k_BT	$k_BT + \Delta G_5$	$\Delta G_7 - \Delta G_{13}$
R6	$C_3H_8(a) + BO_1O^\bullet \rightleftharpoons C_3H_7\text{-}BO_1OH$	C_3H_8 Activation: Dehydrogenation by $BO_1O^\bullet$ Active Site	k_BT	$k_BT + \Delta G_6$	-1.050
R7	$C_3H_7\text{-}BO_1OH + BO_1O^\bullet \rightleftharpoons 2BO_1OH + C_3H_6(a)$	Final Dehydrogenation ($with\ BO_1O^\bullet$)	k_BT	$k_BT + \Delta G_7$	$-0.32 - (\Delta G_8 + \Delta G_9)$

R8	$2BO_1OH \rightleftharpoons BO_1O^{\bullet} + H_2O\text{-}BO_1$	Water Formation	$f_{8f}(\theta_{BO_1OH})$[a]	$f_{8r}(\theta_{BO_1OH})$[a]	$f_{8f} - f_{8r}$
R9	$H_2O\text{-}BO_1 \rightleftharpoons BO_1 + H_2O(a)$	Water Release	$f_{9f}(\theta_{BO_1OH})$[a]	$f_{9r}(\theta_{BO_1OH})$[a]	$f_{9f} - f_{9r}$
R10	$C_3H_6(a) \rightleftharpoons C_3H_6(g)$	C_3H_6 Desorption	unactivated	unactivated	0.490
R11	$H_2O(a) \rightleftharpoons H_2O(g)$	H_2O Desorption	unactivated	unactivated	0.000
Dynamic BO_x Speciation					
R12	$2BO_{1.5} \rightleftharpoons BO_1O^{\bullet} + BO_1$	Dynamic Acive Site Formation	k_BT	$k_BT + \Delta G_{12}$	1.083
R13	$BO_{1.5} + BO_1 \rightleftharpoons BO_2 + BO_{1.5}$	Dangling Bond Attachment	k_BT	$k_BT + \Delta G_{13}$	0.174

[a] These functions are derived from a fitting to the Blue-Moon ensemble AIMD simulations, and their functional forms can be found in Section S2.3 of the SI.

The thermodynamic and kinetic parameters of the MKM are obtained using the reaction dynamics seen in our liquid B_2O_3 AIMD simulations and accounts for the B-OH ($\mathbf{BO_1OH}$) concentration dependence determined for the regeneration of the active sites in the preceding section. To describe global entropy more accurately, the activity coefficient of an ideal lattice gas ($\gamma_i = [\theta_i^{max} - \theta_i]^{-1}$) is used instead of that of an ideal 2D gas ($\gamma_i^{(ideal)} = 1$). This helps account for the disparity in maximum coverages of each species (Table S4), which differ from one another because the liquid nature of the catalyst allows for more or less packing than a fixed lattice would permit. The maximum coverage, θ_i^{max}, is thus dependent upon each species' effective volume of exclusion, which is doubtlessly different for each species. Thermodynamic consistency is carefully maintained throughout. Further details concerning the construction and parameterization of the MKM can be found in Section S2 of the SI.

Many elementary reactions were found to occur spontaneously (< 1 ps) in our AIMD simulations. This indicates that the forward barriers ($\Delta G_{i,f}^{\ddagger}$) of these reactions are no greater than 1 k_BT (~0.07 eV at 823 K), and so this value is used for those reactions' barriers to provide a conservative estimate—making their reverse reaction barriers ($\Delta G_{i,r}^{\ddagger}$) equal to $|\Delta G_i| + k_BT$. This also establishes another constraint on our MKM: such steps must be exergonic ($\Delta G_i < 0$). Only R8 and R9, the formation and release of $\mathbf{H_2O}$ to recover $\mathbf{BO_1O^{\bullet}}$ and $\mathbf{BO_1}$ active sites, have appreciable barriers. Their reaction barriers are taken from a fitting (Section S2.3) of our Blue-Moon ensemble simulation results and vary appropriately as a function of B-OH coverage. The free energies associated with the liquification processes (R12 and R13) were derived from the aforementioned equilibrium constants extracted from the AIMD of the pristine liquid B_2O_3. Since populations are sensitive to even small errors in free energy, we allow ourselves to vary the computed equilibrium constant of R12 up to one order of magnitude during the parameterization process. Since R12 and R13 reactions are in dynamic equilibrium under these conditions, barriers of 1 k_BT and $|\Delta G_i| + k_BT$ are also used.

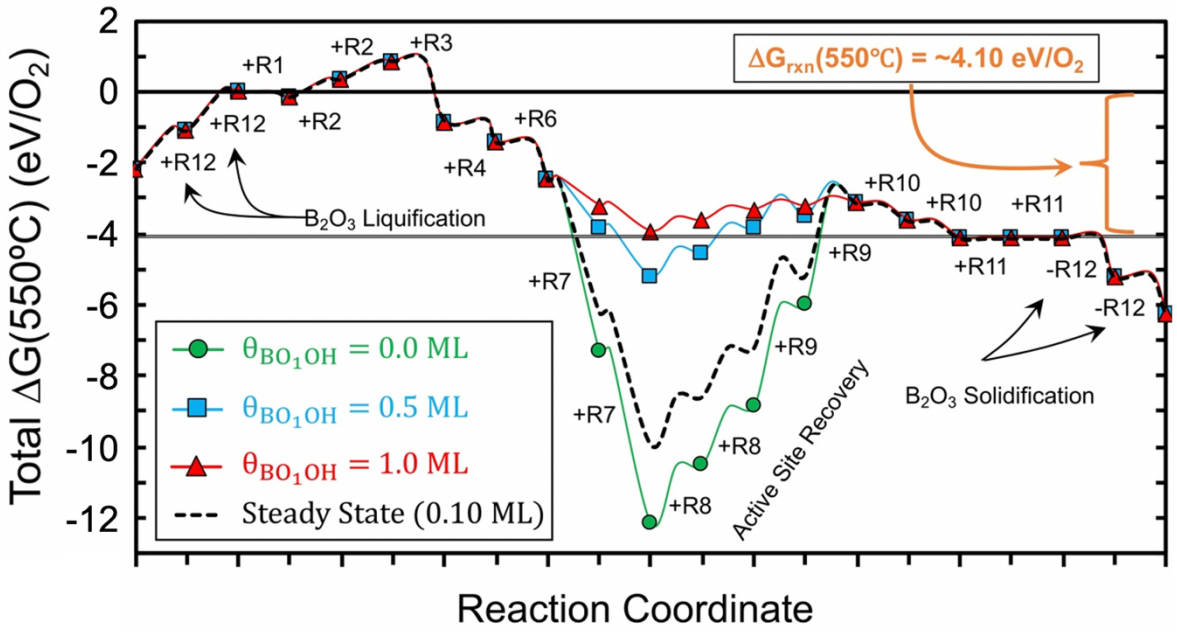

Figure 8. Free energy diagram of ODHP ($2C_3H_8 + O_2 \rightarrow 2C_3H_6 + 2H_2O$) as a function of $\mathbf{BO_1OH}$ (B-OH, previously) coverage. The reaction free energies are directly computed from the underlying species' chemical potentials which were themselves determined by inversion of the system of linear equations representing the interdependent relationships between reaction free energies and species' chemical potentials under thermodynamic and other constraints that can be found in Table S5 of the SI.

The Blue Moon ensemble simulations of H_2O formation (R8) and H_2O removal (R9) show conclusively that their activation barriers are B-OH coverage dependent. However, as is evident in Figure 6 and Figure S23, the difference between their forward and reverse reaction rates are not constant with coverage, resulting in the stated change in equilibrium constant and implying that their reaction free energies (i.e., ΔG_i) are also B-OH concentration dependent. This means that some or all the chemical potentials of the intermediate species involved in R8 and R9 (i.e., $\mathbf{BO_1OH}$, $\mathbf{H_2O/BO_1}$, $\mathbf{BO_1O^\bullet}$, $\mathbf{BO_1}$, and $\mathbf{H_2O(a)}$) must also depend on B-OH concentration. Consequently, the reaction free energy of any *other* reactions involving these same species would likewise be coverage dependent. Given the available data, we choose to keep the number of coverage-dependent chemical potentials at a minimum and allow only $\mathbf{BO_1OH}$ and $\mathbf{H_2O/BO_1}$ chemical potentials to vary with coverage, which results in R5, R7, R8, and R9 having coverage dependent reaction free energies. This is sufficient to reproduce the Blue Moon ensemble results. Applying all thermodynamic and physicality constraints, we arrive at the activation free energies shown in Table 1 and Table S6, and the final values and concentration-dependent expressions we have derived for the underlying chemical potentials can be found in Table S7 of the SI. These dependences must be carefully constrained at all times to maintain thermodynamic consistency across all conditions and coverages to ensure known reaction free energies are recovered and the total reaction's thermodynamics are unaltered. The final reaction pathways (one for each B-OH coverage examined) that result from all

considerations and constraints mentioned herein are shown in Figure 8. R5 is not shown in Figure 8 since it is a parallel reaction to R7 as previously mentioned and would simply run parallel above the reaction pathway shown. The coverage dependence of these reactions manifests as an overall destabilization of $\mathbf{BO_1OH}$ and $\mathbf{H_2O/BO_1}$ species as the $\mathbf{BO_1OH}$ coverage increases, facilitating H_2O formation and removal, which is visually evident in Figure 8.

While all AIMD was carried out at 850 K, the available experimental data only ranges from 803 K to 823 K, so we solve the MKM in this temperature range under the assumption that the free energy/entropy is sufficiently linear with temperature. Nonetheless, we must keep in mind that the MKM is most valid at higher temperatures since that is where AIMD was run. Since conversion and catalyst loading are kept relatively low in experiments, the effect of plug flow, heat generation/removal, and conversion is likely insignificant. Therefore, we can avoid coupling the MKM to a reactor model and instead report the total ODHP rate as the rate of propene formation in the MKM at steady state (i.e., the reaction extent of R10), which is equivalent to the rate of propane consumption here. Due to how rapid most elementary steps are (recall that most only have forward activation free energy barriers of 1 k_BT), only negligible coverages are found for all species except the $\mathbf{BO_1OH}$ and $\mathbf{H_2O/BO_1}$ species, which build up to ~0.10 ML and ~0.11 ML, respectively, at steady state. The remainder is unconverted $\mathbf{BO_{1.5}}$ species.

The apparent activation barrier of the MKM was found by mildly perturbing β ($(k_BT)^{-1}$) to produce an Arrhenius plot, which is shown as green circles in Figure 9A. The corresponding *experimental* Arrhenius plot (orange squares[54]) at the same conditions clearly has two linear regimes: a high temperature regime (blue dashed best-fit line in Figure 9A) with an apparent barrier of ~1.09 eV and a low temperature regime (orange dashed best-fit line in Figure 9A) with apparent barrier of ~2.82 eV. This is clear evidence for a change in mechanism as the temperature increases. Given that the melting point of pure B_2O_3 is typically cited as 723 K[55-56], and that the apparent barrier of the low temperature regime is on the order of those found on non-liquid, crystalline boron-based ODH catalysts[3], it is entirely possible that the low temperature mechanism is consistent with a more solid B_2O_3 phase while the high temperature mechanism coincides with a more liquid B_2O_3 phase. If the maximum coverage of $\mathbf{BO_1OH}$ is set at 0.106 ML, we found that the MKM is able to reproduce precisely the experimental apparent activation barrier of ~1.09 eV. This essentially indicates that global entropy (reflected in the activity coefficient) limits the effects of the coverage-dependence, which is a fascinating finding if this parameterization is reflective of reality. To help validate this and ensure it is not merely a conveniently parameterization, we turn to evaluating reaction rate orders in an attempt to further validate the model.

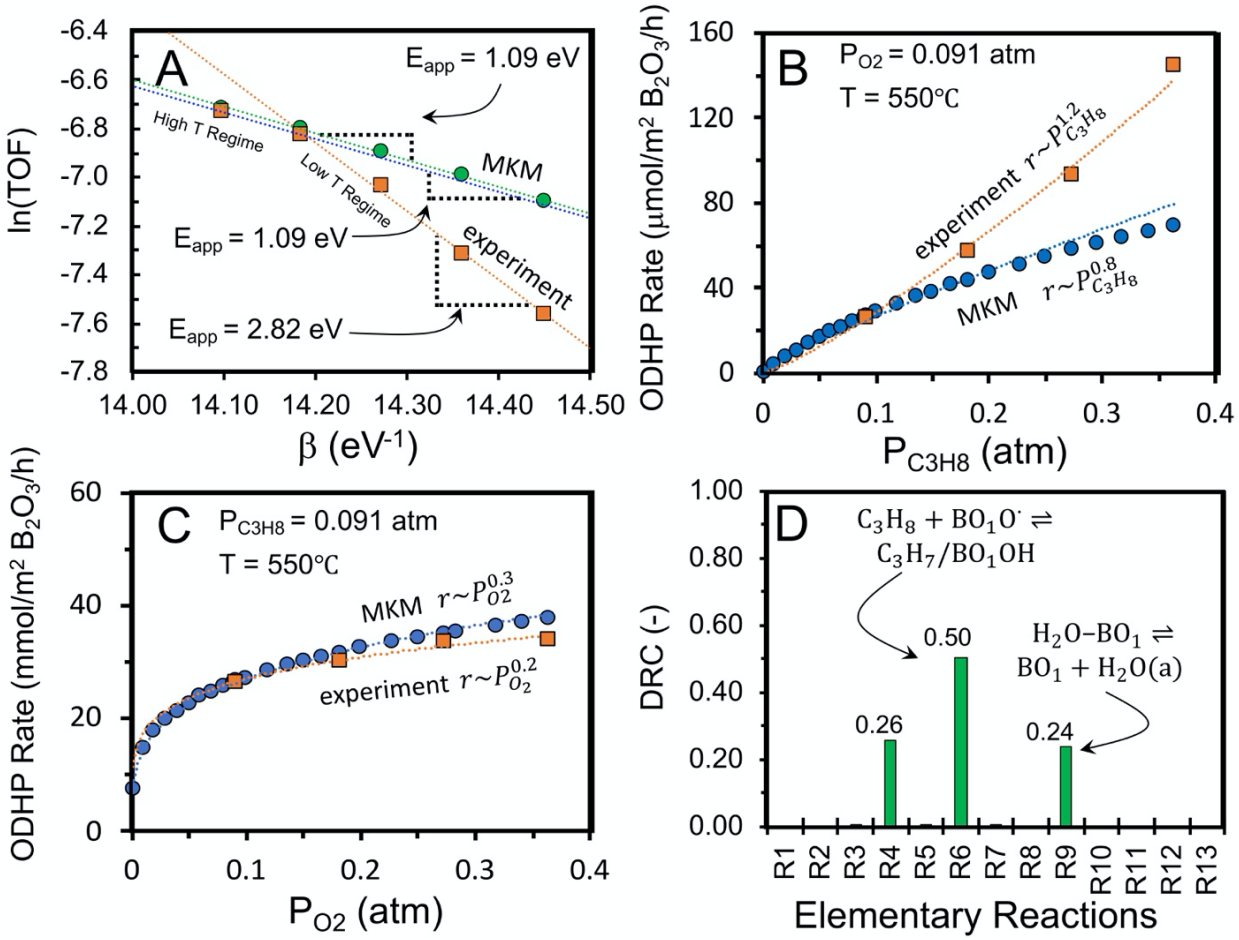

Figure 9. (A) Arrhenius plots revealing the apparent activation barrier of our MKM (green circles) and that determined from experiment (orange squares). The dashed lines are best fit lines. (B-C) MKM (blue circles) and experimental (orange squares) ODHP rate as a function of partial pressures of (B) propane and (C) oxygen. (D) Degree of rate control (DRC) analysis on each elementary reaction in the MKM. The definition of each reaction can be found in **Figure 7** and **Table 1**.

To determine the rate order in $\mathbf{C_3H_8}$ and in $\mathbf{O_2}$, the partial pressures of $\mathbf{C_3H_8}$ and $\mathbf{O_2}$ were varied from effectively 0 to ~0.37 atm while holding the other reactant partial pressure constant at 0.091 atm (balance: inert gas) and recording the resultant steady state ODHP rate. This replicates the experimental protocol. We performed a power law ($r = kP_{O_2}^{n}P_{C_3H_8}^{m}$) fitting to the resulting data to compare against the experimental rate order determination at 823 K (where, as previously discussed, the MKM is most valid). As seen in Figures 9B and 9C, the predicted MKM rates display excellent agreement with experiment as a function of reactant partial pressures. The experimental rate order of ODHP over other boron-based catalysts has been reported to be 2.0 and 0.5 (or Langmuir-type) in $\mathbf{C_3H_8}$ and $\mathbf{O_2}$, respectively[1, 8, 57]. Our experimental rate orders can indeed be fit to a second and half order rate law with reasonable agreement, but fractional exponents nonetheless fit the data much better and so we base correspondence on the non-integer exponents. With this in mind, the rate order in $\mathbf{C_3H_8}$ is fairly underpredicted (exp: ~1.2; MKM:

~0.8) but the rate order in $\mathbf{O_2}$ coincides with experiment remarkably well (exp: ~0.2; MKM: ~0.3). In this sense, the overall agreement is striking and lends credence to our MKM. Like ours, the rate order in $\mathbf{C_3H_8}$ has also been underpredicted in other published MKMs[57], but considering that no published MKM has yet to accurately recover the partial rate order in $\mathbf{O_2}$ as we have done here, we tentatively conclude that we have correctly identified the active site(s) and captured the most important mechanistic aspects of ODHP over liquid B_2O_3 with this MKM. Importantly, it was crucial to increase the endergonicity of B_2O_3 liquification from ~0.54 eV to ~1.08 eV to produce a partial order dependence in $\mathbf{O_2}$. If the B_2O_3 liquification process makes these active sites too readily available, then $\mathbf{O_2}$ is never limited by their availability, which we can conclude is the origin of its rate order. This increase effectively makes the dynamic creation of active sites (R12) less frequent than what was estimated from AIMD population analysis, further showcasing the central importance of the liquid nature of the catalyst.

Importantly, when the C_3H_7* radical desorbs to the gas phase, the gas-phase radical reaction (C_3H_7* + O_2) may occur, which has been reported in the literature[18-20]. The fact that no MKMs have yet to adequately capture the greater-than-unity rate order in propane may be good evidence for the involvement of these ancillary gas-phase propane reactions occurring in the experiment[19], which are often second order[58] and would explain the ostensible but persistent discrepancy between computed and experimental rate orders. Indeed, this was the suggested explanation by Rajbanchi et al.[57], which follows from a detailed study on this phenomenon by Kraus and Lindstedt[19]. Thus, given the available data, we hypothesize that a major portion of the ODHP activity that remains uncaptured in our MKM (Figure 9B) is the result of this gas phase reactivity. Under this hypothesis, the difference between the experimental and MKM-predicted rate indicates that ~40% of the observed ODHP rate comes from gas phase reactions depending on inlet $\mathbf{C_3H_8}$ concentration, which is on the order generally estimated for the oxidative dehydrogenation of other alkenes with other catalysts[59-60]. We regard this aspect as especially relevant to future research into ODHP over liquid B_2O_3 catalysts.

Figure 9D shows the computed degree of rate control (DRC)[61] for each elementary step in the reaction mechanism. Based on this, we found that the ODHP rate is primarily controlled by the activation of propane—firstly by the $\mathbf{BO_1O^\bullet}$ active site (R6, DRC = 0.50), and secondarily by the peroxy $\mathbf{(BO_1)_2O_2}$ active site (R4, DRC = 0.26). The remainder of the rate is controlled by R9, the final active site recovery step, which has a DRC of 0.24, and every other step has a DRC of effectively zero. This result is due to the difficulty of adsorbing propane (R2) which stems from considerable entropy loss upon adsorption. If the equilibrium constant for adsorption favors the gas phase (as is the case here), then the forward propane flux is initially disfavored and is overall dictated by how quickly the first exergonic steps convert adsorbed propane to a (more) stable intermediate. In this case, these are R4 and R6, which convert propane to the more stable $\mathbf{C_3H_7/BO_1OH}$ intermediate, explaining why more than 75% of the rate control comes from

these reactions. The coverage of $\mathbf{BO_1OH}$ species is near saturation, so decreasing the barrier of R9 has a direct, if minor, influence on the rate control. The barrier for R8, the dehydration of $\mathbf{BO_1OH}$ species to form $\mathbf{H_2O(a)}$ and recover the $\mathbf{BO_1O^\bullet}$ active site, is always smaller than R9 within the accessible range of $\mathbf{BO_1OH}$ coverages, explaining why it has no rate control. In other words, the activity of the liquid B_2O_3 catalyst (the high temperature mechanism) has much more to do with the probability that propane will be activated upon impingement before desorbing and less to do with the barriers involved in the subsequent conversion steps (though they are certainly a factor). This shows that one must take caution before identifying a rate controlling step based on barriers alone, particularly in largely anharmonic systems like the liquid catalysts studied here.

Summarily, while the supermajority of our MKM's parameterization was stiffly constrained, we found that the results are critically dependent upon the tuning of three important parameters: (1) the free energy of propane adsorption, (2) the equilibrium constant for dynamic active site formation, and (3) the saturation coverage of B-OH species. Endergonic propane adsorption (R2) is consistent with experiments showing propane adsorption to be difficult even at room temperature,[17] but quantitative data are not available to precisely benchmark our value. On the one hand, this study does link together the disparate observations and mechanisms previously proposed by experiment and theory but further reveals clear avenues of future inquiry and experimental validation that may not be apparent from the current state of the literature. For instance, no data at all are available to compare and benchmark our values for the latter two rate controlling parameters suggesting an opportunity for further investigations to validate these findings through *in situ* spectroscopy and kinetics.

Conclusions

Combined ab initio molecular dynamics, *in situ* Raman characterization, and detailed microkinetic modeling demonstrate that the liquid B_2O_3 has in fact two tandem active sites, a di-coordinated >B* boron site and a B-O* dangling bond, formed simultaneously from the dynamic homolytic cleavage of fully saturated B-O-B bonds at the surface of the liquid B_2O_3 phase. The di-coordinated >B* site (specifically a pair of them) is responsible for activating O_2 molecules by forming a non-dissociative peroxy-like >B-O-O-B< complex, which itself acts as a moderate oxidant capable of activating adsorbed propane while exhibiting no activity for deeper oxidation. The dynamically formed >B-O* dangling bonds are also capable of activating propane but are found to be most essential to abstracting H from C_3H_7* radical species to form the C_3H_6 product and boron hydroxyls, B-OH. The dehydration of B-OH and subsequent desorption of H_2O to recover the active sites and close the catalytic cycle is a strong function of B-OH concentration. These two steps were found to be the only activated steps in the reaction mechanism at 850 K. Active site recovery

would thus be rate determining if propane adsorption were favorable. In fact, we find that only about one quarter of the rate is controlled by dehydration of B-OH to form and desorb H_2O, while the remaining three quarters of the rate is controlled by propane activation. As others have also reported, we find strong evidence that the desorption of C_3H_7* radical species leads to radical initiated gas phase reactions.

This study shows very conclusively that the liquification of B_2O_3 catalysts is essential to reducing the apparent activation barrier for ODHP. However, at the elevated temperatures needed to melt the catalyst material, reactant adsorption becomes less favorable, such that the majority of the rate is controlled by propane activation, which is the only mechanism by which propane can accumulate on the surface otherwise. Nonetheless, we find that about one quarter of the rate is controlled by the highly endergonic reaction barriers associated with active site recovery from otherwise extremely stable boron hydroxyls. Finally, our study suggests that the simplest and most effective ways to enhance the ODHP rate over liquid B_2O_3 catalysts is to (1) improve propane adsorption and (2) increase the coverage of B-OH species. However, if our results are correct, the system already operates at the saturation coverage of B-OH during steady state and would thus resist further increases in B-OH coverage, making improving the adsorption of propane the likely more effective approach.

Methods

Computational Methods

DFT parameters. All DFT calculations were performed using the CP2K package[62-63]. The exchange-correlation energy was described by the generalized-gradient approximation with spin-polarized Perdew–Burke–Ernzerhof functional[64]. The wavefunctions were expanded in an optimized double-z Gaussian basis sets with an auxiliary plane wave basis set with a cutoff energy of 400 Rydberg[65]. Core electrons have been modelled by scalar relativistic norm-conserving pseudo potentials[66] with 3, 6, 1 and 4 valence electrons for B, O, H and C, respectively. Brillouin zone integration is performed with a reciprocal space mesh consisting of only the gamma point. The convergence criterion for the maximum force is set as 4×10^{-4} atomic units.

Computational models. The geometry optimization of crystalline B_2O_3-I (4×4×2 supercell) was initially performed using the BFGS algorithm, relaxing both the lattice parameters and the atomic coordinates. We found the optimized unit cell parameters of crystalline B_2O_3-I to be $a = b = 4.36$ Å and $c = 8.51$ Å, which are in good agreement with experimental values ($a = b = 4.34$ Å, and $c = 8.34$ Å with $\alpha = \beta = 90^o$, $\gamma = 120°$)[40]. A B_2O_3 (101) surface structure was designed by cleaving the B_2O_3-I bulk structure. The lattice parameters of constructed B_2O_3(101), consisted of 480 atoms (192B+288O) atoms, are determined to be a = 19.2Å, b = 17.467Å, and c = 50 Å ($\alpha = \beta = 90^o$, $\gamma = 103.137°$) with a vacuum space of 35 Å in the z direction.

AIMD simulations. All *ab initio* MD simulations were performed by sampling the NVT canonical ensemble employing Nose-Hoover thermostats[67-68] with a time step of 0.5 fs at a finite temperature. To obtain a liquid state, we begin by carrying out AIMD at temperatures of 2000 and 1500 K for 12 ps each starting from B_2O_3-I (101) face. The temperature is selected to be high enough to make the system reach a completely disordered state without the effects of the initial configuration. Then, we decrease the temperature of the system gradually from 1000 K to the final target temperature of 850 K running for another 20 ps, respectively. The vibrational density of states (VDOS) was calculated for predicting the spectroscopic characteristics based on the Fourier transform of the velocity autocorrelation function using[69-70].

$$D(\omega) = \int_0^\infty e^{-i\omega t}(\upsilon(\tau) \times \upsilon(\tau + t))dt \quad (1)$$

where υ is defined as the velocity and the angular brackets represent the statistical average over time. This allows us to properly describe the anharmonicity of systems at a given temperature. Further partial VDOS (pVDOS) based on each atom type leads to the accurate interpretation of the associated peaks in the vibrational bands.

The Blue-Moon ensemble method[71] was used to evaluate free energy barriers of H_2O formation from B-OH species (the cleavage of O-H bond) and H_2O desorption from the surface (the cleavage of B-O bond). For H_2O formation, the O-H distance between two B-OH ($R_{O\text{-}H}$) was chosen to be the collective variable while B-O_{H2O} distance was chosen for H_2O desorption. By constraining distance between two given atoms, the corresponding Lagrange multipliers, λ, can be integrated over the distances to determine free energy starting from initial distance and ending once the barrier has been surmounted, via

$$\Delta G = \int_{R_{C-O}^{init}}^{R_{C-O}^{TS}} \langle \lambda_{R_{C-O}} \rangle dR_{C-O} \quad (2)$$

where $\langle \lambda_{R_{C-O}} \rangle$ is the statistical average value of the $\lambda_{R_{C-O}}$ at each constrained point in the Blue-Moon ensemble simulation.

Microkinetic Modeling

Like most microkinetic models (MKMs) of heterogenous catalytic systems[72-75], the elementary reaction rates involving surface bound species were described via Transition State Theory[76], which defines the rate as:

$$r_i = \frac{k_B T}{h} \exp\left(-\beta \Delta G_i^{\ddagger}\right) \prod_n^{\text{IS Species}} \theta_n \gamma_n \quad (4)$$

where r_i is the forward or backward reaction rate of elementary reaction i; k_B and h are the Boltzmann and

Plank constants, respectively; T is the absolute temperature; β is the thermodynamic beta ($[k_B T]^{-1}$); $\Delta G_i^{\ddagger}$ is the activation free energy of elementary reaction i; and θ_n and γ_n are the coverage and activity coefficient of the n^{th} initial state (IS) species involved in the elementary reaction. Note that we at all times satisfy local thermodynamic consistency by ensuring that the difference between forward and reverse reaction free energy barriers recovers the free energy of reaction: $\Delta G_{i,fwd}^{\ddagger} - \Delta G_{i,rev}^{\ddagger} = \Delta G_i$. To impose natural bounds on the species' coverages, we define the activity coefficient as that of an ideal lattice gas[77] [ref]:

$$\gamma_n = (\theta_n^{max} - \theta_n)^{-1} \quad (5)$$

where θ_n^{max} is the maximum or saturation coverage of species n and more accurately reflects the loss in entropy as species' coverages approach their maximum value. At low coverages, γ_n tends toward the usual ideal 2D gas activity coefficient of unity (i.e., $\gamma_n^{(ideal)} = 1$) when $\theta_n^{max} = 1.0$ ML.

Based on the AIMD simulations performed, we see no evidence for activated adsorption or desorption events, justifying the use of standard adsorption and desorption rate expressions[78-81]. That is, the adsorption rate of species n is given as

$$S_0\left(\theta_n^{max} - \theta_j\right)\frac{a_{u.c.}P_n}{\sqrt{2\pi m_n k_B T}} \quad (6)$$

and its desorption rate is given as

$$S_0(\theta_n^{max} - \theta_n)\frac{k_B T}{h}\left(\frac{a_{u.c.}}{\lambda_n^2}\right)e^{\beta(\Delta G_{ads,n})}(\theta_n \gamma_n) \quad (7)$$

where S_0 is the sticking coefficient, taken to be unity here; $a_{u.c.}$ is the area of a unit cell within our system (~27.3 Å^2); P_n, m_n, λ_n, and $\Delta G_{ads,n}$ are the partial pressure, mass, thermal wavelength ($\lambda_n = \left[\frac{h^2}{2\pi m_n k_B T}\right]^{\frac{1}{2}}$), and adsorption energy of species, n, respectively.

More details concerning the construction and parameterization of the MKM reported here can be found in the Section S2 of the SI.

Experimental Characterization

***in situ* Raman spectra**. *in situ* Raman characterization was performed with Renishaw RT 1000 and Dilor LabRam I microprobe Raman systems equipped with CCD detector using a home-built high-temperature *in situ* Raman cell designed for the microprobe Raman spectrometer. The samples were placed in a sample holder equipped with a thermocouple placed below the holder for temperature measurement. The excitation wavelength was a 532.5 nm solid laser with a power of ~4 mW measured at the analysis spot. The temperature of the Raman cell was then raised from room temperature (RT) to ~850 K. The Raman spectra of the catalyst were recorded at selected temperatures during this process.

***in situ* Fourier transform infrared spectra** (*in situ* FT-IR). *in situ* FT-IR were recorded under different

conditions on a Nicolet 6700 FT-IR spectrometer equipped with mercury cadmium telluride (MCT) detector. The 32.8%B_2O_3/SiO_2 catalysts of ~20 mg was compressed as a thin disk (diameter = 1.0 cm) and placed in a transmission cell equipped with KBr windows. We designed three experiments including i) the catalyst was first pretreated in He flow at ~470K for 2 h, and then cooled down to RT. After that, the spectra were scanned in the range 600-4000 cm^{-1} with a 2 cm^{-1} resolution from RT to 850K; ii) the system was vacuumed at 850K and the spectra were collected; iii) the gas feed of C_3H_8:O_2:He with 1:1:9 at 33 mL/min was introduced at 850K for 10 min and then the system was vacuumed again and the spectra were collected at different time.

ORCID

Jinshu Tian: https://orcid.org/0000-0003-0033-4636

Greg Collinge: http://orcid.org/0000-0001-8345-6254

Simuck F. Yuk: https://orcid.org/0000-0003-1355-4400

Jingdong Lin: http://orcid.org/0000-0003-0686-6908

Vassiliki-Alexandra Glezakou: https://orcid.org/0000-0001-6028-7021

Mal-Soon Lee: https://orcid.org/0000-0001-6851-177X

Yong Wang: http://orcid.org/0000-0002-8460-7410

Roger Rousseau: https://orcid.org/0000-0003-1947-0478

Acknowledgements

This work was supported by the US Department of Energy (DOE) Office of Science, Office of Basic Energy Sciences, Division of Chemical Sciences, Geosciences and Biosciences catalysis program (FWP #47319) and the National Natural Science Foundation of China (No. 22072119, and 51802281). PNNL is a multiprogram national laboratory operated by Battelle for DOE. Computational work was performed using the Molecular Sciences Computing Facility (MSCF) in the William R. Wiley Environmental Molecular Sciences Laboratory, a US Department of Energy (DOE) national scientific user facility sponsored by the DOE's Office of Biological and Environmental Research and located and the Pacific Northwest National Laboratory (PNNL) and the National Energy Research Scientific Computing Center (NERSC), a U.S. Department of Energy, Office of Science User Facility located at Lawrence Berkley National Laboratory provided by a user proposal.

References

1. Grant, J.; Carrero, C. A.; Goeltl, F.; Venegas, J.; Mueller, P.; Burt, S. P.; Specht, S.; McDermott, W.; Chieregato, A.; Hermans, I., Selective Oxidative Dehydrogenation of Propane to Propene Using Boron Nitride Catalysts. *Science* **2016,** *354* (6319), 1570-1573.
2. Grant, J. T.; McDermott, W. P.; Venegas, J. M.; Burt, S. P.; Micka, J.; Phivilay, S. P.; Carrero, C. A.; Hermans, I., Boron and Boron‐Containing Catalysts for the Oxidative Dehydrogenation of Propane. *ChemCatChem* **2017,** *9* (19), 3623-3626.
3. Shi, L.; Wang, D.; Song, W.; Shao, D.; Zhang, W.-P.; Lu, A.-H., Edge-Hydroxylated Boron Nitride for Oxidative Dehydrogenation of Propane to Propylene. *ChemCatChem* **2017,** *9* (10), 1788-1793.
4. Zhou, H.; Yi, X.; Hui, Y.; Wang, L.; Chen, W.; Qin, Y.; Wang, M.; Ma, J.; Chu, X.; Wang, Y., Isolated Boron in Zeolite for Oxidative Dehydrogenation of Propane. *Science* **2021,** *372* (6537), 76-80.
5. Wang, T.-C.; Yin, J.-L.; Guo, X.-J.; Chen, Y.; Lang, W.-Z.; Guo, Y.-J., Modulating the Crystallinity of Boron Nitride for Propane Oxidative Dehydrogenation. *J. Catal.* **2021,** *393*, 149-158.
6. Liu, Z.; Yan, B.; Meng, S.; Liu, R.; Lu, W. D.; Sheng, J.; Yi, Y.; Lu, A. H., Plasma Tuning Local Environment of Hexagonal Boron Nitride for Oxidative Dehydrogenation of Propane. *Angew. Chem. Int. Ed.* **2021,** *60* (36), 19691-19695.
7. Dorn, R. W.; Cendejas, M. C.; Chen, K.; Hung, I.; Altvater, N. R.; McDermott, W. P.; Gan, Z.; Hermans, I.; Rossini, A. J., Structure Determination of Boron-Based Oxidative Dehydrogenation Heterogeneous Catalysts with Ultrahigh Field 35.2 T ^{11}b Solid-State Nmr Spectroscopy. *ACS Catal.* **2020,** *10* (23), 13852-13866.
8. Lu, W.-D.; Wang, D.; Zhao, Z.; Song, W.; Li, W.-C.; Lu, A.-H., Supported Boron Oxide Catalysts for Selective and Low-Temperature Oxidative Dehydrogenation of Propane. *ACS Catal.* **2019,** *9* (9), 8263-8270.
9. Buyevskaya, O.; Müller, D.; Pitsch, I.; Baerns, M., Selective Oxidative Conversion of Propane to Olefins and Oxygenates on Boria-Containing Catalysts. *Stud. Surf. Sci. Catal.* **1998,** *119*, 671-676.
10. Liu, Q.; Wu, Y.; Xing, F.; Liu, Q.; Guo, X.; Huang, C., B_2o_3@ Bpo_4 Sandwich-Like Hollow Spheres as Metal-Free Supported Liquid-Phase Catalysts. *J. Catal.* **2020,** *381*, 599-607.
11. Lenoir, D., Selective Oxidation of Organic Compounds-Sustainable Catalytic Reactions with Oxygen and without Transition Metals? *Angew. Chem. Int. Ed.* **2006,** *45* (20), 3206-3210.
12. North, M., *Sustainable Catalysis: Without Metals or Other Endangered Elements, Part 2*. Royal Society of Chemistry: 2015.
13. Bullock, R. M.; Chen, J. G.; Gagliardi, L.; Chirik, P. J.; Farha, O. K.; Hendon, C. H.; Jones, C. W.; Keith, J. A.; Klosin, J.; Minteer, S. D.; Morris, R. H.; Radosevich, A. T.; Rauchfuss, T. B.; Strotman, N. A.; Vojvodic, A.; Ward, T. R.; Yang, J. Y.; Surendranath, Y., Using Nature's Blueprint to Expand Catalysis with Earth-Abundant Metals. *Science* **2020,** *369* (6505).
14. Love, A. M.; Thomas, B.; Specht, S. E.; Hanrahan, M. P.; Venegas, J. M.; Burt, S. P.; Grant, J. T.; Cendejas, M. C.; McDermott, W. P.; Rossini, A. J., Probing the Transformation of Boron Nitride Catalysts under Oxidative Dehydrogenation Conditions. *J. Am. Chem. Soc.* **2018,** *141* (1), 182-190.
15. Venegas, J. M.; McDermott, W. P.; Hermans, I., Serendipity in Catalysis Research: Boron-Based Materials for Alkane Oxidative Dehydrogenation. *Acc. Chem. Res.* **2018,** *51* (10), 2556-2564.
16. Shi, L.; Wang, D.; Lu, A.-H., A Viewpoint on Catalytic Origin of Boron Nitride in Oxidative Dehydrogenation of Light Alkanes. *Chinese Journal of Catalysis* **2018,** *39* (5), 908-913.
17. Huang, R.; Zhang, B.; Wang, J.; Wu, K. H.; Shi, W.; Zhang, Y.; Liu, Y.; Zheng, A.; Schlögl, R.; Su, D. S., Direct Insight into Ethane Oxidative Dehydrogenation over Boron Nitrides. *ChemCatChem* **2017,** *9* (17), 3293-3297.
18. Venegas, J. M.; Zhang, Z.; Agbi, T. O.; McDermott, W. P.; Alexandrova, A.; Hermans, I., Why Boron Nitride Is Such a Selective Catalyst for the Oxidative Dehydrogenation of Propane. *Angew. Chem. Int. Ed.* **2020,** *59* (38), 16527-16535.
19. Kraus, P.; Lindstedt, R. P., It'sa Gas: Oxidative Dehydrogenation of Propane over Boron Nitride Catalysts. *J. Phys. Chem. C* **2021,** *125* (10), 5623-5634.

20. Zhang, X.; You, R.; Wei, Z.; Jiang, X.; Yang, J.; Pan, Y.; Wu, P.; Jia, Q.; Bao, Z.; Bai, L., Radical Chemistry and Reaction Mechanisms of Propane Oxidative Dehydrogenation over Hexagonal Boron Nitride Catalysts. *Angew. Chem. Int. Ed.* **2020,** *59* (21), 8042-8046.
21. Tian, J.; Tan, J.; Xu, M.; Zhang, Z.; Wan, S.; Wang, S.; Lin, J.; Wang, Y., Propane Oxidative Dehydrogenation over Highly Selective Hexagonal Boron Nitride Catalysts: The Role of Oxidative Coupling of Methyl. *Sci. Avd.* **2019,** *5* (3), eaav8063.
22. Krogh-Moe, J., The Structure of Vitreous and Liquid Boron Oxide. *Journal of Non-Crystalline Solids* **1969,** *1* (4), 269-284.
23. Zhang, Z.; Jimenez-Izal, E.; Hermans, I.; Alexandrova, A. N., Dynamic Phase Diagram of Catalytic Surface of Hexagonal Boron Nitride under Conditions of Oxidative Dehydrogenation of Propane. *J. Phys. Chem. Lett.* **2018,** *10* (1), 20-25.
24. Altvater, N. R.; Dorn, R. W.; Cendejas, M. C.; McDermott, W. P.; Thomas, B.; Rossini, A. J.; Hermans, I., B-Mww Zeolite: The Case against Single-Site Catalysis. *Angewandte Chemie International Edition* **2020,** *132* (16), 6608-6612.
25. McDermott, W. P.; Cendejas, M. C.; Hermans, I., Recent Advances in the Understanding of Boron-Containing Catalysts for the Selective Oxidation of Alkanes to Olefins. *Top. Catal.* **2020,** *63*, 1700-1707.
26. Yan, H.; Alayoglu, S.; Wu, W.; Zhang, Y.; Weitz, E.; Stair, P. C.; Notestein, J. M., Identifying Boron Active Sites for the Oxidative Dehydrogenation of Propane. *ACS Catal.* **2021,** *11* (15), 9370-9376.
27. Si, C.; Lian, Z.; Olanrele, S. O.; Sun, X.; Li, B., Revealing the Origin of the Reactivity of Metal-Free Boron Nitride Catalysts in Oxidative Dehydrogenation of Propane. *Appl. Surf. Sci.* **2020,** *519*, 146241.
28. White, C. E.; Provis, J. L.; Proffen, T.; Riley, D. P.; Van Deventer, J. S., Combining Density Functional Theory (Dft) and Pair Distribution Function (Pdf) Analysis to Solve the Structure of Metastable Materials: The Case of Metakaolin. *Phys. Chem. Chem. Phys.* **2010,** *12* (13), 3239-3245.
29. Zhang, Z.; Cui, Z.-H.; Jimenez-Izal, E.; Sautet, P.; Alexandrova, A. N., Hydrogen Evolution on Restructured B-Rich Wb: Metastable Surface States and Isolated Active Sites. *ACS Catal.* **2020,** *10* (23), 13867-13877.
30. Zandkarimi, B.; Alexandrova, A. N., Surface-Supported Cluster Catalysis: Ensembles of Metastable States Run the Show. *WIREs Computational Molecular Science* **2019,** *9* (6).
31. Zhang, Z.; Zandkarimi, B.; Alexandrova, A. N., Ensembles of Metastable States Govern Heterogeneous Catalysis on Dynamic Interfaces. *Acc. Chem. Res.* **2020,** *53* (2), 447-458.
32. Sun, G.; Sautet, P., Metastable Structures in Cluster Catalysis from First-Principles: Structural Ensemble in Reaction Conditions and Metastability Triggered Reactivity. *J. Am. Chem. Soc.* **2018,** *140* (8), 2812-2820.
33. Collinge, G.; Yuk, S. F.; Nguyen, M.-T.; Lee, M.-S.; Glezakou, V.-A.; Rousseau, R., Effect of Collective Dynamics and Anharmonicity on Entropy in Heterogenous Catalysis: Building the Case for Advanced Molecular Simulations. *ACS Catal.* **2020,** *10* (16), 9236-9260.
34. Marx, D.; Hutter, J., Ab Initio Molecular Dynamics: Theory and Implementation. *Modern methods and algorithms of quantum chemistry* **2000,** *1* (301-449), 141-152.
35. Wang, Y.-G.; Mei, D.; Glezakou, V.-A.; Li, J.; Rousseau, R., Dynamic Formation of Single-Atom Catalytic Active Sites on Ceria-Supported Gold Nanoparticles. *Nat. Commun.* **2015,** *6* (1), 1-8.
36. Yang, G.; Akhade, S. A.; Chen, X.; Liu, Y.; Lee, M. S.; Glezakou, V. A.; Rousseau, R.; Lercher, J. A., The Nature of Hydrogen Adsorption on Platinum in the Aqueous Phase. *Angew. Chem. Int. Ed.* **2019,** *58* (11), 3527-3532.
37. Piccini, G.; Lee, M.-S.; Yuk, S. F.; Zhang, D.; Collinge, G.; Kollias, L.; Nguyen, M.-T.; Glezakou, V.-A.; Rousseau, R., Ab Initio Molecular Dynamics with Enhanced Sampling in Heterogeneous Catalysis. *Catal. Sci. Technol.* **2021**.
38. Motagamwala, A. H.; Dumesic, J. A., Microkinetic Modeling: A Tool for Rational Catalyst Design. *Chem. Rev.* **2020,** *121* (2), 1049-1076.
39. Marin, G. B.; Yablonsky, G. S.; Constales, D., *Kinetics of Chemical Reactions: Decoding Complexity*. John Wiley & Sons: 2019.

40. Assaf, N. W.; De La Pierre, M.; Altarawneh, M. K.; Radny, M. W.; Jiang, Z.-T.; Dlugogorski, B. Z., Structure, Stability, and (Non) Reactivity of the Low-Index Surfaces of Crystalline B_2O_3–I. *J. Phys. Chem. C* **2017,** *121* (21), 11346-11354.
41. Huang, L.; Durandurdu, M.; Kieffer, J., New B_2O_3 Crystals Predicted from Concurrent Molecular Dynamics Simulations and First-Principles Calculations. *J. Phys. Chem. C* **2007,** *111* (37), 13712-13720.
42. Ferlat, G.; Charpentier, T.; Seitsonen, A. P.; Takada, A.; Lazzeri, M.; Cormier, L.; Calas, G.; Mauri, F., Boroxol Rings in Liquid and Vitreous B_2O_3 from First Principles. *Phys. Rev. Lett.* **2008,** *101* (6), 65504-65510.
43. Zahn, K.; Lenke, R.; Maret, G., Two-Stage Melting of Paramagnetic Colloidal Crystals in Two Dimensions. *Phys. Rev. Lett.* **1999,** *82* (13), 2721.
44. Samantaray, M.; Sarangi, S., Melting Phenomena of $Cu_{0.25}Ni_{0.75}$ Bimetallic Alloy: A Molecular Dynamics Approach. *Mater. Today: Proc.* **2021**.
45. Ohmura, S.; Shimojo, F., Mechanism of Atomic Diffusion in Liquid B_2O_3: An Ab Initio Molecular Dynamics Study. *Phys. Rev. B* **2008,** *78* (22), 224206-2242122.
46. Simon, G.; Hehlen, B.; Vacher, R.; Courtens, E., Hyper-Raman Scattering Analysis of the Vibrations in Vitreous Boron Oxide. *Phys. Rev. B* **2007,** *76* (5), 54210-54220.
47. Bader, R. F. W., Everyman's Derivation of the Theory of Atoms in Molecules. *J. Phys. Chem. A* **2007,** *111* (32), 7966-7972.
48. Yu, M.; Trinkle, D. R., Accurate and Efficient Algorithm for Bader Charge Integration. *J. Chem. Phys.* **2011,** *134* (6), 064111.
49. Henkelman, G.; Arnaldsson, A.; Jónsson, H., A Fast and Robust Algorithm for Bader Decomposition of Charge Density. *Comput. Mater. Sci.* **2006,** *36* (3), 354-360.
50. Sanville, E.; Kenny, S. D.; Smith, R.; Henkelman, G., Improved Grid-Based Algorithm for Bader Charge Allocation. *J. Comput. Chem.* **2007,** *28* (5), 899-908.
51. Tang, W.; Sanville, E.; Henkelman, G., A Grid-Based Bader Analysis Algorithm without Lattice Bias. *J. Phys.: Condens. Matter* **2009,** *21* (8), 084204.
52. Zhou, Y.; Lin, J.; Li, L.; Pan, X.; Sun, X.; Wang, X., Enhanced Performance of Boron Nitride Catalysts with Induction Period for the Oxidative Dehydrogenation of Ethane to Ethylene. *J. Catal.* **2018,** *365*, 14-23.
53. Collinge, G.; Kruse, N.; McEwen, J.-S., Role of Carbon Monoxide in Catalyst Reconstruction for Co Hydrogenation: First-Principles Study of the Composition, Structure, and Stability of Cu/Co (1012) as a Function of Co Pressure. *J. Phys. Chem. C* **2017,** *121* (4), 2181-2191.
54. Tian, J.; Li, J.; Qian, S.; Zhang, Z.; Wan, S.; Wang, S.; Lin, J.; Wang, Y., Understanding the Origin of Selective Oxidative Dehydrogenation of Propane on Boron-Based Catalysts. *Appl. Catal. A* **2021**, 118271-118279.
55. Franck, E. U., Homogeneous and Heterogeneous Electron Transfer Rates of the Tetrathiafulvalene-System. *Ber. Bunsenges. Phys. Chem.* **1990,** *94* (1), 92-93.
56. L.V. Gurvich; Veyts, I. V.; Iorish, V. S.; C.B. Alcock, Thermodynamic Properties of Individual Substances. 4th ed.; Hemisphere Pub. Corp.: New York :, 1994; Vol. 3, pp 1-716.
57. Rajbanshi, B.; Saha, S.; Fricke, C.; Ammal, S. C.; Heyden, A., Oxidative Dehydrogenation of Propane on the Oxygen Adsorbed Edges of Boron Nitride Nanoribbons. *Catal. Sci. Technol.* **2020,** *10* (15), 5181-5195.
58. Westley, F. *Table of Recommended Rate Constants for Chemical Reactions Occurring in Combustion*; National Standard Reference Data System: 1980.
59. Kung, H. H., Oxidative Dehydrogenation of Light (C_2 to C_4) Alkanes. *Adv. Catal.* **1994,** *40*, 1-38.
60. Burch, R.; Crabb, E. M., Homogeneous and Heterogeneous Contributions to the Catalytic Oxidative Dehydrogenation of Ethane. *Appl. Catal. A* **1993,** *97* (1), 49-65.
61. Campbell, C. T., The Degree of Rate Control: A Powerful Tool for Catalysis Research. ACS Publications: 2017; Vol. 7, pp 2770-2779.
62. Lippert, G.; Hutter, J.; Parrinello, M., The Gaussian and Augmented-Plane-Wave Density Functional Method for Ab Initio Molecular Dynamics Simulations. *Theor. Chem. Acc.* **1999,** *103* (2), 124-

140.
63. VandeVondele, J.; Krack, M.; Mohamed, F.; Parrinello, M.; Chassaing, T.; Hutter, J., Quickstep: Fast and Accurate Density Functional Calculations Using a Mixed Gaussian and Plane Waves Approach. *Comput. Phys. Commun.* **2005,** *167* (2), 103-128.
64. Perdew, J. P.; Burke, K.; Ernzerhof, M., Generalized Gradient Approximation Made Simple. *Phys. Rev. Lett.* **1996,** *77* (18), 3865-3873.
65. VandeVondele, J.; Hutter, J., Gaussian Basis Sets for Accurate Calculations on Molecular Systems in Gas and Condensed Phases. *J. Chem. Phys.* **2007,** *127* (11), 114105-114115.
66. Goedecker, S.; Teter, M.; Hutter, J., Separable Dual-Space Gaussian Pseudopotentials. *Phys. Rev. B* **1996,** *54* (3), 1703-1712.
67. Hoover, W. G., Canonical Dynamics: Equilibrium Phase-Space Distributions. *Phys. Rev. A* **1985,** *31* (3), 1695-1705.
68. Nosé, S., A Unified Formulation of the Constant Temperature Molecular Dynamics Methods. *J. Chem. Phys.* **1984,** *81* (1), 511-519.
69. Gaigeot, M.-P.; Martinez, M.; Vuilleumier, R., Infrared Spectroscopy in the Gas and Liquid Phase from First Principle Molecular Dynamics Simulations: Application to Small Peptides. *Mol. Phys.* **2007,** *105* (19-22), 2857-2878.
70. Yuk, S. F.; Lee, M.-S.; Collinge, G.; Zhang, J.; Padmaperuma, A. B.; Li, Z.; Polo-Garzon, F.; Wu, Z.; Glezakou, V.-A.; Rousseau, R., Mechanistic Understanding of Catalytic Conversion of Ethanol to 1-Butene over 2d-Pillared Mfi Zeolite. *J. Phys. Chem. C* **2020,** *124* (52), 28437-28447.
71. Sprik, M.; Ciccotti, G., Free Energy from Constrained Molecular Dynamics. *J. Chem. Phys.* **1998,** *109* (18), 7737-7744.
72. Eyring, H., The Activated Complex in Chemical Reactions. *J. Chem. Phys.* **1935,** *3* (2), 107-115.
73. Besora, M.; Maseras, F., Microkinetic Modeling in Homogeneous Catalysis. *Wiley Interdiscip. Rev. Comput. Mol. Sci.* **2018,** *8* (6), 1372-1385.
74. Cortright, R.; Dumesic, J., Kinetics of Heterogeneous Catalytic Reactions: Analysis of Reaction Schemes. *Adv. Catal.* **2001,** *46*, 161-264.
75. Gokhale, A. A.; Kandoi, S.; Greeley, J. P.; Mavrikakis, M.; Dumesic, J. A., Molecular-Level Descriptions of Surface Chemistry in Kinetic Models Using Density Functional Theory. *Chem. Eng. Sci.* **2004,** *59* (22-23), 4679-4691.
76. Laidler, K. J.; King, M. C., The Development of Transition-State Theory. *J. Chem. Phys.* **1983,** *87* (15), 2657-2664.
77. Campbell, C. T.; Sprowl, L. H.; Árnadóttir, L. n., Equilibrium Constants and Rate Constants for Adsorbates: Two-Dimensional (2d) Ideal Gas, 2d Ideal Lattice Gas, and Ideal Hindered Translator Models. *J. Phys. Chem. C* **2016,** *120* (19), 10283-10297.
78. Kreuzer, H. J., Kinetics of Adsorption, Desorption and Reactions at Surfaces. In *Springer Handbook of Surface Science*, Springer: 2020; pp 1035-1052.
79. Payne, S.; McEwen, J.-S.; Kreuzer, H. J.; Menzel, D., Adsorption and Desorption of Co on Ru (0 0 0 1): A Comprehensive Analysis. *Surf. Sci.* **2005,** *594* (1-3), 240-262.
80. Wong, B. M.; Collinge, G.; Hensley, A. J.; Wang, Y.; McEwen, J.-S., Benchmarking the Accuracy of Coverage-Dependent Models: Adsorption and Desorption of Benzene on Pt (1 1 1) and Pt_3sn (1 1 1) from First Principles. *Prog. Surf. Sci.* **2019,** *94* (2), 100538-100547.
81. Che, F.; Ha, S.; McEwen, J.-S., Hydrogen Oxidation and Water Dissociation over an Oxygen-Enriched Ni/Ysz Electrode in the Presence of an Electric Field: A First-Principles-Based Microkinetic Model. *Ind. Eng. Chem. Res.* **2017,** *56* (5), 1201-1213.